J. Mech. Phys. Solids 214 (2026) 106688

Contents lists available at ScienceDirect

Journal of the Mechanics and Physics of Solids

journal homepage: www.elsevier.com/locate/jmps

# Nucleation in rank-one gradient plasticity: Exact solutions and geometry-dependent regimes

Maria Chiara Comella [a], Antonino Favata [a,*], Andrea Rodella [b,c], Stefano Vidoli [a]

[a] Department of Structural and Geotechnical Engineering, Sapienza University of Rome, Rome, Italy
[b] Université Paris-Saclay, CEA, SRMA, Gif-sur-Yvette, 91191, France
[c] Institut Jean Le Rond ∂'Alembert, Sorbonne Université and CNRS, UMR 7190, Paris, 75252, France

ARTICLE INFO

*Keywords:*
Gradient plasticity
Positively one-homogeneous defect energy
Plastic nucleation
Plastic support
Variational methods
Internal length scale

ABSTRACT

We investigate plastic nucleation in solids within a strain-gradient plasticity framework featuring a rank-one defect energy, formulated as an incremental convex variational problem. The designation *rank-one* refers to the fact that the defect energy is positively one-homogeneous with respect to the curl of the plastic strain. The core feature of the framework is the variational selection of the plastic support, which regularizes the singular localization of classical plasticity into a distributed nucleus of finite width and introduces a genuine strengthening effect: the yield threshold is elevated by a discrete energetic barrier, while the post-yield response remains perfectly plastic. For an annular domain under azimuthal shear, we identify two qualitatively distinct nucleation regimes governed by the interplay between the internal length scale and the domain geometry. In the first regime, plasticity spreads over the entire domain in a curl-free compatible configuration. In the second, it localizes in an inner nucleus sealed by a concentrated geometric necessary dislocations wall at a locked front that does not advance upon further loading. Closed-form analytical solutions are derived for both regimes without any a priori assumption on the plastic support, providing exact benchmarks for the numerical simulations. In the localized regime, both the plastic zone size and the yield threshold follow a square-root scaling law in the internal length scale, in contrast to the linear scaling of previous rank-one models where the plastic support is prescribed by microstructural constraints. Numerical simulations on elliptical geometries show that the scaling exponents and the nucleation pattern depend sensitively on the domain shape, identifying geometry as a control variable of the nucleation process on a par with the internal length scale.

## 1. Introduction

The mechanical behavior of materials at small scales often reveals a pronounced size-dependent response, summarized by the "smaller is stronger" paradigm. These effects, which elude classical continuum theories, have been extensively investigated through experiments such as the torsion of micro-wires and the bending of thin foils (Fleck et al., 1994; Hutchinson, 2000). To address these observations, strain-gradient plasticity (SGP) frameworks have been developed, extending the classical constitutive response

* Corresponding author.
*E-mail addresses:* mariachiara.comella@uniroma.it (M.C. Comella), antonino.favata@uniroma.it (A. Favata), andrea.rodella@cea.fr (A. Rodella), stefano.vidoli@uniroma.it (S. Vidoli).

https://doi.org/10.1016/j.jmps.2026.106688
Received 19 March 2026; Received in revised form 30 April 2026; Accepted 18 May 2026
Available online 20 May 2026

by introducing internal length scales that relate higher-order gradients of the plastic fields to the material's energetic and dissipative behavior (Gurtin, 2003; Fleck and Willis, 2009).

A fundamental aspect of SGP is the energetic storage associated with lattice defects, particularly geometrically necessary dislocations (GNDs). In the small-strain, plastically irrotational framework developed by Gurtin and Anand (Gurtin and Anand, 2005; Anand et al., 2005), the density of GNDs is directly related to the incompatibility of the plastic strain field, typically measured by the curl of the plastic strain $\mathbf{E}^{\mathrm{p}}$. Most established models regularize the response by assuming a defect energy that is quadratic in $|\operatorname{curl}\mathbf{E}^{\mathrm{p}}|$. While these quadratic regularizations provide mathematical closure and align with several experimental trends (Giacomini, 2012; Panteghini and Bardella, 2016, 2018; Lewintan et al., 2021), they inherently produce smooth plastic strain distributions. By construction, they primarily act as hardening mechanisms and do not shift the initial yield threshold, which remains local and independent of the internal length scale. This lack of influence on the onset of plasticity is particularly notable in benchmark problems involving simple shear and torsion, as investigated in Chiricotto et al. (2012, 2016) and Bardella and Panteghini (2015), Panteghini and Bardella (2020).

From a rigorous mathematical standpoint, the study of rate-independent systems and the existence of energetic solutions in SGP has been considered by Lussardi and Giacomini (2008), Giacomini (2012).

In this context, the physical origin of defect energy can be traced back to the Read–Shockley model for crystal grain boundaries (Read and Shockley, 1950), where the energetic cost scales linearly with the dislocation density or misorientation angle. This physical ground has motivated the exploration of defect energies that are positively one-homogeneous (rank-one) with respect to $|\operatorname{curl}\mathbf{E}^{\mathrm{p}}|$, a concept that naturally emerges from the homogenization of discrete dislocations and the study of non-convex energy minimization (Ortiz and Repetto, 1999; Conti and Ortiz, 2005; Garroni et al., 2010; Reddy, 2011; Fortuna et al., 2025).

Rank-one defect energies were pioneered by Ohno and Okumura (2007), who related higher-order stresses to the self-energy of GNDs, and have since been explored in Forest and Guéninchault (2013), Wulfinghoff et al. (2015), Jebahi and Forest (2023) and Bardella (2010), Panteghini et al. (2019), Bardella (2021) in the context of gradient crystal plasticity and laminates. In these configurations, the support of the plastic incompatibility is tied to prescribed microstructural features — grain size or slip plane spacing — leading to an energetic penalty linear in the internal length and a correspondingly linear scaling of the yield threshold.

The core novelty of the present work lies in moving beyond prescribed-support configurations by adopting a purely variational framework in which the *spatial extent of the plasticized region* is itself an optimization variable. This shift has several consequences that we summarize here and develop in detail throughout the paper.

*Nucleation barrier and strengthening.* The rank-one defect energy introduces a *structural nucleation barrier*: activating a plastic zone of finite width requires overcoming a discrete energetic threshold, resulting in a genuine shift of the yield stress rather than a hardening effect. Once nucleated, the plastic zone evolves at constant stress — a perfectly plastic post-yield response — in contrast to the progressive hardening produced by quadratic models.

*Two nucleation regimes.* For an annular domain under azimuthal shear, the variational selection of the plastic support is conveniently analyzed through a dual formulation, which introduces a bounded micro-stress field that encodes the resistance of the GND distribution to further plastic slip. The admissibility of this field within its bounds determines two qualitatively distinct nucleation regimes. When the annulus is sufficiently thin, the micro-stress remains strictly within its bounds and the energetically optimal solution spreads plasticity over the entire domain in a curl-free, compatible configuration (regime A). When the annulus is wider, sustaining a globally compatible solution would require the micro-stress to exceed its bound: the system instead localizes plasticity in an inner nucleus, sealed by a concentrated GND wall at a locked front, where the micro-stress saturates with vanishing derivative (regime B). The transition between the two regimes depends on the ratio between the internal length and the domain size, and is sharp: arbitrarily close to the critical geometry, the nucleation pattern changes discontinuously from a fully compatible plastic flow to a localized nucleus of finite width. In both regimes, closed-form analytical solutions are derived, providing exact benchmarks for the numerical simulations.

*Square-root scaling and locked front.* In regime B, both the incipient plastic zone size and the yield threshold follow a square-root scaling law in the internal length scale. Once nucleated, the plastic front does not advance upon further loading: plastic strain accumulates within the fixed support while the front position remains locked. This contrasts with the point-like localization of classical perfect plasticity and the continuously expanding front of quadratic SGP models. It also clarifies that the linear scaling reported in previous rank-one studies (Ohno and Okumura, 2007; Wulfinghoff et al., 2015) is a consequence of microstructural constraints — where the support of the plastic incompatibility is prescribed by grain size or slip plane spacing — rather than a fundamental property of the rank-one energy.

*Geometry-dependent nucleation.* Numerical simulations on elliptical geometries demonstrate that the scaling exponents and the spatial pattern of plastic nucleation depend sensitively on the domain shape. The geometry of the domain is therefore a control variable of the nucleation process on a par with the internal length itself.

*Incremental consistency.* The incremental convex variational structure avoids the spurious elastic-gap phenomenon that arises in the non-incremental SGP theories, where gradient contributions enter the dissipation potential (Panteghini et al., 2019; Nielsen and Hutchinson, 2021). We remark that, as shown by Fleck and Willis (2015), elastic gaps can arise also in incremental formulations when non-local terms appear in the dissipation rather than in the free energy. In the present model, no gradient contribution is included in the dissipation, and the numerical simulations of Section 8 confirm the absence of elastic gaps under non-proportional loading for the configurations considered.

The article is organized as follows. Section 2 presents the 3D variational formulation. Section 3 introduces the 1D axisymmetric benchmark. Section 4 recovers the classical von Mises solution. Section 5 analyzes the quadratic defect energy. Section 6 derives the analytical solutions for the rank-one model, including the two nucleation regimes and the scaling laws. Section 7 reviews and

compares the main results obtained. Section 8 presents numerical results for circular and elliptical geometries. Section 9 provides conclusions and perspectives.

## 2. Three-dimensional variational formulation

It is well known that the problem of infinitesimal, rate-independent associate perfect plasticity admits a variational formulation (see, for instance, Mielke (2005)). Specifically, given a bounded Lipschitz domain $\Omega \subset \mathbb{R}^3$ with boundary $\partial\Omega$, the solution at time $t$ is obtained through the following minimization problem:

$$\min_{\mathbf{u}\in\mathscr{U}_t,\mathbf{E}^{\mathrm{p}}\in\mathscr{P}} \mathscr{E}_t^{\mathrm{p}}(\mathbf{u},\mathbf{E}^{\mathrm{p}}), \tag{1}$$

where the functional

$$\mathscr{E}_t^{\mathrm{p}}(\mathbf{u},\mathbf{E}^{\mathrm{p}}) = \frac{1}{2}\int_\Omega \mathbb{C}[\mathbf{E}-\mathbf{E}^{\mathrm{p}}]\cdot(\mathbf{E}-\mathbf{E}^{\mathrm{p}})\,\mathrm{d}\mathbf{x} + \sqrt{2}\,\tau_Y \int_\Omega \int_0^t |\dot{\mathbf{E}}^{\mathrm{p}}(s)|\,\mathrm{d}s\,\mathrm{d}\mathbf{x}, \tag{2}$$

represents the sum of the stored elastic energy and the plastic dissipation up to time $t$. This functional is minimized with respect to the displacement field $\mathbf{u}$ and the plastic strain field $\mathbf{E}^{\mathrm{p}}$. In (2), $\mathbb{C}$ is the isotropic elasticity tensor, $\mathbf{E} = \operatorname{sym}\nabla\mathbf{u}$ is the infinitesimal strain, and $\tau_Y$ is the *yield stress* under shear.

In this formulation, we omit body forces and tractions in favor of a hard-device loading condition, where the displacement must satisfy a prescribed time-dependent value $\bar{\mathbf{u}}(t)$ on a subset of the boundary $\partial\Omega_D \subset \partial\Omega$. Namely:

$$\mathscr{U}_t := \left\{\mathbf{u}\in\mathscr{U} \,:\, \mathbf{u} = \bar{\mathbf{u}}(t) \text{ on } \partial\Omega_D\right\}. \tag{3}$$

We will discuss the regularity requirement of the functional spaces $\mathscr{U}$ and $\mathscr{P}$ for the displacement and plastic strain, respectively, in a later section. However, our analysis is limited to the case of von Mises plasticity, where $\operatorname{tr}\mathbf{E}^{\mathrm{p}} = 0$; thus, the elements of $\mathscr{P}$ are deviatoric tensor fields on $\Omega$.

Building upon this setting, we consider energetic contributions that penalize incompatibilities in the plastic strain via terms depending on $\operatorname{curl}\mathbf{E}^{\mathrm{p}}$. Their physical origin is rooted in continuum dislocation theory (Nye, 1953; Kröner, 1958; Bilby et al., 1955). Specifically, a non-vanishing $\operatorname{curl}\mathbf{E}^{\mathrm{p}}$ signals the presence of geometrically necessary dislocations (GNDs), which arise to accommodate spatially non-uniform plastic deformations (Ashby, 1970; Fleck et al., 1994). At the microscopic level, dislocations are line defects characterized by a Burgers vector that measures the lattice mismatch induced by plastic slip. In a continuum setting, the net Burgers vector content per unit area is represented by the Kröner–Nye dislocation density tensor $(\operatorname{curl}\mathbf{E}^{\mathrm{p}})^{\mathsf{T}}$, which quantifies the geometrically necessary dislocation content of the plastic deformation field (Nye, 1953; Kröner, 1958; Gurtin, 2002). Within a small-strain, plastically irrotational framework, the symmetric part of $\operatorname{curl}\mathbf{E}^{\mathrm{p}}$ serves as the primary measure of plastic incompatibility. Energetic penalizations of $|\operatorname{curl}\mathbf{E}^{\mathrm{p}}|$ thus represent the stored energy associated with the elastic distortion fields induced by the GND network, in the spirit of the self-energy of a dislocation distribution (Read and Shockley, 1950; Gurtin, 2003).

We consider both quadratic and rank-one penalizations of the tensor field $\operatorname{curl}\mathbf{E}^{\mathrm{p}}$ via the following minimization problems:

$$\min_{\mathbf{u}\in\mathscr{U}_t,\,\mathbf{E}^{\mathrm{p}}\in\mathscr{P}} \left(\mathscr{E}_t^{\mathrm{gp}2}(\mathbf{u},\mathbf{E}^{\mathrm{p}}) := \mathscr{E}_t^{\mathrm{p}}(\mathbf{u},\mathbf{E}^{\mathrm{p}}) + \frac{\mu}{2}a^2\int_\Omega |\operatorname{curl}\mathbf{E}^{\mathrm{p}}|^2\,\mathrm{d}\mathbf{x}\right), \tag{4}$$

and

$$\min_{\mathbf{u}\in\mathscr{U}_t,\,\mathbf{E}^{\mathrm{p}}\in\mathscr{P}} \left(\mathscr{E}_t^{\mathrm{gp}1}(\mathbf{u},\mathbf{E}^{\mathrm{p}}) := \mathscr{E}_t^{\mathrm{p}}(\mathbf{u},\mathbf{E}^{\mathrm{p}}) + \mu\,\ell\int_\Omega |\operatorname{curl}\mathbf{E}^{\mathrm{p}}|\,\mathrm{d}\mathbf{x}\right). \tag{5}$$

Here, $a$ and $\ell$ are two characteristic lengths, and $\mu$ is the shear modulus associated with $\mathbb{C}$. To avoid overloading the notation, we employ the same symbols for the functional spaces $\mathscr{U}$ and $\mathscr{P}$ of the three problems (1), (4) and (5); however, the regularity requirements for the well-posedness of these problems vary across the three cases.

The quadratic defect energy in (4) originates from the microforce balance framework introduced by Gurtin (2003) and further developed by Anand and Gurtin for isotropic, plastically irrotational materials (Gurtin and Anand, 2005; Anand et al., 2005).[1]

The rank-one defect energy in (5) is derived from the homogenization of discrete dislocations within the framework of non-convex energy minimization (Ortiz and Repetto, 1999; Conti and Ortiz, 2005; Garroni et al., 2010; Reddy, 2011; Fortuna et al., 2025). This formulation is consistent with the Read–Shockley scaling of defect energy (Read and Shockley, 1950), where the energetic cost scales linearly with the dislocation density or misorientation angle. Since the GND density is proportional to $|\operatorname{curl}\mathbf{E}^{\mathrm{p}}|$ in the continuum setting (Nye, 1953; Kröner, 1958), this linear scaling motivates a defect energy that is positively one-homogeneous in $|\operatorname{curl}\mathbf{E}^{\mathrm{p}}|$, rather than quadratic.

**Remark 1.** In the perfect plasticity model (1), no intrinsic length scale is present and plastic yielding is entirely local. In contrast, both models (4) and (5) introduce a characteristic length. Consequently, both exhibit size-effects and can be classified as gradient plasticity models.

[1] In Gurtin's original models, a dissipative length was introduced alongside the energetic internal length $a$. To disentangle the roles of energetic and dissipative regularizations, we do not consider the gradient contribution in the plastic dissipation.

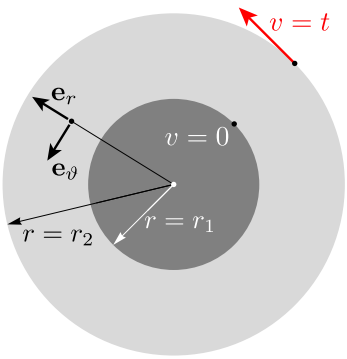


**Fig. 1.** Geometry and boundary conditions of the axisymmetric annular problem.

**Remark 2.** A fundamental difference between the two gradient plasticity models in (4) and (5) is evident under monotonic loading from a state of vanishing plastic strain. The yield in (4) does not depend on $a$, whereas the yield in (5) is affected by $\ell$. Indeed, at $\mathbf{E}^{\mathrm{p}} = \mathbf{0}$, the directional derivative of the quadratic penalization term vanishes, while this is not the case for the rank-one penalization term.

**Remark 3.** From a computational perspective, the rank-one penalization in (5) is non-smooth, as the absolute value is non-differentiable when its argument vanishes. However, it poses numerical challenges that are in some respects more severe than those of the cumulated plastic strain in (1). While both involve non-smooth terms, the rank-one penalization is non-local, since it involves $\operatorname{curl}\mathbf{E}^{\mathrm{p}}$ rather than $\mathbf{E}^{\mathrm{p}}$ pointwise. This non-local non-smoothness causes standard Newton–Raphson solvers to fail, and requires the use of dedicated conic optimization methods, as discussed in Section 8.

## 3. A one-dimensional problem: geometry and energetics

In this section we introduce a planar benchmark problem with elementary geometry, which nevertheless captures the essential features of the models introduced and admits analytical solutions. The reference configuration is a circular annulus with inner radius $r_1$ and outer radius $r_2$. On the inner boundary of the annulus, a homogeneous Dirichlet boundary condition is prescribed $\mathbf{u}(r = r_1) = \mathbf{0}$, corresponding to a fully clamped inner surface. On the outer boundary a purely tangential displacement is imposed,

$$\mathbf{u}(r = r_2) = t\,\mathbf{e}_\vartheta, \qquad t \geq 0,$$

which induces a azimuthal shear deformation of the annulus. Under monotonically increasing load, the parameter $t \geq 0$ parametrizes the temporal evolution of the system.

We adopt here a system of cylindrical curvilinear coordinates $(r, \vartheta, z)$ and the associated orthonormal basis $\mathbf{e}_r, \mathbf{e}_\vartheta, \mathbf{e}_z = \mathbf{e}_r \times \mathbf{e}_\vartheta$, as illustrated in Fig. 1. The problem is invariant along the $z$-direction, and all fields are independent of the angular coordinate $\vartheta$.

Owing to the axisymmetry of the geometry and boundary conditions, the displacement field possesses a single nonvanishing component and can be written as

$$\mathbf{u}(r, \vartheta) = v(r)\,\mathbf{e}_\vartheta(\vartheta), \tag{6}$$

where $v(r)$ denotes the amplitude of the circumferential displacement. Hence, the linearized total strain tensor reduces to a pure shear contribution and takes the form

$$\mathbf{E}(r, \vartheta) = \gamma(r)\left(\mathbf{e}_r \otimes \mathbf{e}_\vartheta + \mathbf{e}_\vartheta \otimes \mathbf{e}_r\right), \quad \gamma(r) := \frac{1}{2}\left(v'(r) - \frac{v(r)}{r}\right), \tag{7}$$

with $\gamma$ the total shear strain and the prime represents derivation with respect to $r$. The plastic strain tensor inherits the same symmetry and is therefore characterized by a single scalar function $p(r)$ as

$$\mathbf{E}^{\mathrm{p}}(r, \vartheta) = p(r)\left(\mathbf{e}_r \otimes \mathbf{e}_\vartheta + \mathbf{e}_\vartheta \otimes \mathbf{e}_r\right). \tag{8}$$

Accordingly, the elastic shear strain is defined as the difference between the total and plastic contributions, namely $\gamma^{\mathrm{e}}(r) := \gamma(r) - p(r)$.

The incompatibility associated with the plastic deformation is measured by the curl of the plastic strain tensor, which using (8) reads

$$\operatorname{curl}\mathbf{E}^{\mathrm{p}}(r, \vartheta) = \left(2\,\frac{p(r)}{r} + p'(r)\right)\mathbf{e}_z \otimes \mathbf{e}_r. \tag{9}$$

Assuming an isotropic material, the stress tensor also inherits the same structure

$$\mathbf{T}(r, \vartheta) = \mathbb{C}(\mathbf{E} - \mathbf{E}^{\mathrm{p}}) = \tau(r)\left(\mathbf{e}_r \otimes \mathbf{e}_\vartheta + \mathbf{e}_\vartheta \otimes \mathbf{e}_r\right), \tag{10}$$

being simply defined by the shear stress $\tau = 2\mu\,\gamma^{\mathrm{e}}$.

Within this reduced setting, the evolution problem means to compute at every instant both the displacement field $v(r)$ and the plastic strain field $p(r)$ for the three models described in the previous section. We perform this computation assuming a sufficiently fine time discretization $t \in [0, t_1, t_2, \dots, t_i, \dots]$, such that for $t > t_i$ and $\mathbf{E}^{\mathrm{p}}$ defined as in (8):

$$\int_0^t |\dot{\mathbf{E}}^{\mathrm{p}}(s)|\,\mathrm{d}s = \sqrt{2}\int_0^t |\dot{p}(s)|\,\mathrm{d}s \simeq \sqrt{2}\int_0^{t_i} |\dot{p}(s)|\,\mathrm{d}s + \sqrt{2}|p(t) - p(t_i)|; \tag{11}$$

here we make explicit the time dependence of the fields $\mathbf{E}^{\mathrm{p}}$ and $p$, rather than the usual spatial dependence.

Using (7), (8), (10), and (11), the three problems discussed in Section 2 reduce to the following sequential ($i = 0, 1, 2, \dots$) minimization problems. On denoting by $p_i := p(t_i)$ the plastic strain field at the previous time step $t_i$, we have for *perfect plasticity*

$$\min_{v\in\mathscr{V}_i,\, p\in\mathscr{P}} \hat{\mathscr{E}}_i^{\mathrm{p}}(v,p) = \int_{r_1}^{r_2} r\left[2\mu\left(\frac{1}{2}\left(v' - \frac{v}{r}\right) - p\right)^2 + 2\tau_Y\,|p - p_i|\right]\mathrm{d}r, \tag{12}$$

for *gradient plasticity with quadratic defect energy*

$$\min_{v\in\mathscr{V}_i,\, p\in\mathscr{P}} \hat{\mathscr{E}}_i^{\mathrm{gp2}}(v,p) = \hat{\mathscr{E}}_i^{\mathrm{p}}(v,p) + \frac{\mu a^2}{2}\int_{r_1}^{r_2} r\left(2\,\frac{p}{r} + p'\right)^2 \mathrm{d}r, \tag{13}$$

and for *gradient plasticity with rank-one defect energy*

$$\min_{v\in\mathscr{V}_i,\, p\in\mathscr{P}} \hat{\mathscr{E}}_i^{\mathrm{gp1}}(v,p) = \hat{\mathscr{E}}_i^{\mathrm{p}}(v,p) + \mu\ell\int_{r_1}^{r_2} r\left|2\,\frac{p}{r} + p'\right|\mathrm{d}r. \tag{14}$$

Here, the functionals $\hat{\mathscr{E}}^{\mathrm{p}}$, $\hat{\mathscr{E}}^{\mathrm{gp2}}$, and $\hat{\mathscr{E}}^{\mathrm{gp1}}$ have been normalized by $2\pi$. In all cases, we start from $p = 0$ at $t = 0$, meaning $p_i = 0$ for $i = 0$. Moreover, we introduce the functional space

$$\mathscr{V}_i := \left\{v \in \mathscr{V},\quad v(r_1) = 0,\ v(r_2) = t_i\right\}, \tag{15}$$

imposing the time-dependent boundary conditions to the circumferential displacement. The regularity of the functional space $\mathscr{V}$ is discussed in the following remark.

**Remark 4.** The well-posedness of the minimization problems (12)–(14) relies on distinct regularity assumptions for the displacement and plastic strain fields. In (12), the appropriate space $\mathscr{P}$ is the space of finite signed Radon measures $\mathscr{M}$, allowing the plastic strain $p$ to exhibit Dirac concentrations. To ensure finite elastic energy, the elastic shear strain must be square integrable $\gamma^e \in L^2$; since $p$ may be singular, the total strain $\gamma$ must match these singularities, requiring the displacement field $v$ to admit jumps. Thus, $v$ belongs to the space of functions of Bounded Variation ($BV$). Conversely, in (13), the finite quadratic defect energy enforces $p \in \mathscr{P} \equiv H^1$, the Sobolev space of functions with square-integrable derivatives. This smoothness extends to the displacement, so $v \in \mathscr{V} \equiv H^1$ as well. Finally, (14) presents an intermediate regime where $\mathscr{P} \equiv BV$ and $\mathscr{V} \equiv H^1$. Here, the plastic strain can undergo finite jumps, but the displacement field remains continuous. In the cases where $p \in \mathscr{M}$ or $BV$, derivatives are understood in the weak sense.

In the following sections, we examine the one-dimensional solutions for the problem of Fig. 1 in Section 3, specifically comparing those derived from perfect plasticity (12), the quadratic defect energy (13), and the rank-one defect energy (14). Our analysis concludes by highlighting the fundamental distinctions in how each model characterizes the solution for the problem at hand in Section 7.

For a fixed plastic strain $p$, each model under consideration reduces to a convex elasticity problem in terms of the displacement $v$. Minimization with respect to $v$ yields a consistent balance equation across all formulations:

$$2\,\frac{\tau(r)}{r} + \tau'(r) = 0, \quad \text{in } [r_1, r_2]. \tag{16}$$

Solving this differential equation implies for the shear stress the form:

$$\tau(r) = \tau_m\,\frac{r_1^2}{r^2}, \tag{17}$$

where $\tau_m$ is a constant, possibly dependent on $t$, determined by the prescribed boundary conditions. Note that $|\tau_m|$ physically means the maximal stress value in the domain $[r_1, r_2]$. Owing to the convexity of the energy functionals, this shear stress distribution is unique. It serves as a universal mechanical driving force, the effects of which are modulated by the specific plastic regularization chosen for each model.

## 4. Solution to the 1D problem: perfect von Mises plasticity

We consider the minimization problem in (12). Minimality with respect to $v$ is fulfilled by a shear stress of the form (17).

A necessary condition for the minimality of $\hat{\mathscr{E}}_i^{\mathrm{p}}$ with respect to the plastic strain $p$ is the non-negativity of the directional derivative:

$$\partial\hat{\mathscr{E}}_i^{\mathrm{p}}(p)(\tilde{p}) = \int_{\Omega_0} 2r\left(\tau_Y\,|\tilde{p}| - \tau\tilde{p}\right)\mathrm{d}r + \int_{\Omega_1} 2r\left(\tau_Y\,\frac{(p - p_i)}{|p - p_i|} - \tau\right)\tilde{p}\,\mathrm{d}r \geq 0, \tag{18}$$

where $\Omega_0$ and $\Omega_1$ are the disjoint subsets of $[r_1, r_2]$ where $p \equiv p_i$ and $p \neq p_i$ respectively and $\tilde{p}$ is an arbitrary admissible perturbation. Choosing suitable perturbations $\tilde{p}$ vanishing first in $\Omega_0$ and then in $\Omega_1$, this inequality implies the classical yield conditions on the shear stress:

$$\begin{cases} \tau = \tau_Y, & \text{where } p > p_i, \\ |\tau| \leq \tau_Y, & \text{where } p = p_i, \\ \tau = -\tau_Y, & \text{where } p < p_i. \end{cases} \tag{19}$$

Therefore, the maximal shear stress is bounded: $|\tau_m(t)| \leq \tau_Y$ for any load $t$.

Hence, we must distinguish two cases: the elastic phase, say $0 \leq t \leq t_c$, where $p = p_i = 0$ everywhere, and the plastic phase, say $t_c < t$, where at least at one point the plastic strain evolves $p \neq p_i = 0$. Here, $t_c$ is a critical threshold for the load $t$, which parametrizes the boundary conditions.

*Elastic phase*

We have $p(r, t) = 0$, and using the constitutive relation and the boundary conditions in (15), the shear stress is given by

$$\tau(r) = \frac{2\mu\,\rho\,r_1}{\rho^2 - 1}\,\frac{t}{r^2}, \qquad 0 \leq t \leq t_c, \tag{20}$$

where $\rho := r_2/r_1 > 1$. It is monotonically decreasing along the radial direction and linearly proportional to the load $t$. The corresponding displacement is $v(r, t) = \rho\, t\big(r^2 - r_1^2\big)/(r\, r_1(\rho^2 - 1))$.

Since for our assumptions the shear stress is positive, the end of the elastic phase is reached when the maximal stress, *i.e.* $\tau(r_1)$ on the inner boundary, reaches the yield value $+\tau_Y$; the threshold load $t_c$ is then

$$t_c = r_1\,\frac{(\rho^2 - 1)}{2\rho}\,\frac{\tau_Y}{\mu}. \tag{21}$$

*Plastic phase*

For the geometry considered and a perfectly plastic material, a plastic zone of finite width cannot exist. Indeed, inside a plasticized region, the yield condition would require $|\tau(r)| = \tau_Y$, but such a constant stress field cannot satisfy the equilibrium Eq. (16), which prescribes a $1/r^2$ decay. Consequently, when $t \geq t_c$, the plastic deformation is forced to localize into a point-singularity at the inner boundary. In the plastic phase, $p$ is hence expressed by a Dirac delta measure in $r = r_1$:

$$p(r) = P\,\delta(r - r_1), \quad t \geq t_c, \tag{22}$$

where $P$ is the intensity of the plastic strain concentration.

To ensure a finite elastic energy, the elastic strain must remain square integrable: $(\gamma - p) \in L^2$. In other words, the plastic strain singularity must be matched by the singular part of the strain $\gamma = v'/2 - v/(2r)$. If the displacement jumps at $r = r_1$, we have:

$$\text{singular part of } (\gamma - p) = \left[\frac{1}{2}[\![v]\!]_{r_1} - P\right]\delta(r - r_1), \tag{23}$$

with $[\![v]\!]_{r_1} := v(r_1^+) - v(r_1^-)$. Hence the energy is finite when this last singular part vanishes *i.e.* when $[\![v]\!]_{r_1} = 2P$.

We can determine the displacement field by solving the balance Eq. (16) with the conditions $v(r_1^+) = 2P$ and $v(r_2) = t$. We find that the shear stress is

$$\tau(r) = \frac{2\mu\,\rho\,r_1}{\rho^2 - 1}\,\frac{t_c}{r^2}, \quad t > t_c, \tag{24}$$

remaining constant, independently of the load $t$, at the critical distribution where $\tau(r_1) \equiv \tau_Y$. Also the absolutely continuous part of the strain also remains fixed at $t = t_c$. Instead, for $t > t_c$ the displacement jump in $r = r_1$ and the amplitude of the plastic strain singularity increase proportionally to $(t - t_c)$:

$$\frac{1}{2}[\![v]\!]_{r_1} = P = \frac{1}{2\rho}\,(t - t_c). \tag{25}$$

In the next sections, we show that the introduction of the defect energies resolves the plastic strain singularity by allowing for a stress overshoot, $|\tau| > \tau_Y$, which in turn enables the variational selection of a plastic support having non-vanishing width.

## 5. Solution to the 1D problem: gradient plasticity with quadratic defect energy

We now consider the same loading problem for the functional (13). Having added the quadratic cost for incompatibilities, both the plastic strain and the displacement are constrained to be more regular, $p \in H^1$ and $v \in H^1$, and, in particular, are continuous in $[r_1, r_2]$.

Clearly, the elastic phase, where plastic strains vanishe everywhere, is identical to the one described in the previous section. Also, the load threshold $t_c$ remains the same as in (21). However, for $t > t_c$ plasticity can now spread over a region of non-vanishing size and the maximal stress is unbounded.

Indeed, from the minimality of $\hat{\mathscr{E}}^{\mathrm{gp2}}$ in (13) with respect to $p$, we find that in the region where plasticity evolves, the following non-local yield equation must be valid:

$$2r^2(\tau_Y - \tau(r)) + \mu\, a^2\Big(4p(r) - rp'(r) - r^2p''(r)\Big) = 0, \tag{26}$$

with the natural boundary condition $2p(r_1) + r_1p'(r_1) = 0$ and $p(r_q) = 0$. This latter condition arises from the continuity of $p$ at the boundary, say $r = r_q$, of the plastic region. Due to the monotonically decreasing character in $r$ of the shear stress distribution, we have found it natural to assume for the plastic region the interval $[r_1, r_q]$, where the end point $r_q \in (r_1, r_2]$ has to be determined as a function of the load $t$.

Since the dependence of the shear stress on the radial component is known from (17), we can solve (26) for $p$ as a function of the maximal shear stress $\tau_m$:

$$p(r) = \frac{\tau_Y}{8\,\mu a^2\, r^2}\left\{(r_q^4 - r^4) + 4\,r^4\log r - 4\,r_q^4\log r_q + 4(r_q^4 - r^4)\log r_1 + 2\,\frac{\tau_m}{\tau_Y}\,(r_q^2 - r^2)(r^2 - 2r_1^2 + r_q^2)\right\}, \tag{27}$$

in $[r_1, r_q]$, while $p = 0$ in $[r_q, r_2]$. To close the problem and determine $\tau_m$ and $r_q$, we must now compute the displacement $v$, inverting the constitutive relation $v' - v/r = 2p + \tau/\mu$ and using the boundary conditions $v(r_1) = 0$ and $v(r_2) = t$, but also optimize the energy functional with respect to $r_q$.

Specifically, we split the determination of the displacement field into two fields: $v_{\mathrm{in}}(r)$ for $r \in [r_1, r_q]$, where $p$ is given by (27) with the boundary condition $v_{\mathrm{in}}(r_1) = 0$, and $v_{\mathrm{out}}(r)$ for $r \in [r_q, r_2]$, where $p = 0$ with the boundary condition $v_{\mathrm{out}}(r_2) = t$. Hence, since $v \in H^1$, by enforcing the continuity of the displacement field at the end of the plastic region $v_{\mathrm{in}}(r_q) = v_{\mathrm{out}}(r_q)$, we determine the maximal shear stress

$$\frac{\tau_m}{\tau_Y} = \frac{4ta^2r_1^2(\rho^2 - 1)/t_c - \rho^2\Big(r_q^4 + 3r_1^4 - 4r_1^2r_q^2\Big) - 4\rho^2r_q^2\Big(r_q^2 - 2r_1^2\Big)\log\frac{r_1}{r_q}}{4a^2(\rho^2 - 1)r_1^2 + 2\rho^2\Big(r_q^4 + 3r_1^4 - 4r_1^2r_q^2\Big) + 8\rho^2r_1^4\log\frac{r_q}{r_1}}. \tag{28}$$

The analytical expressions for $v_{\mathrm{in}}$ and $v_{\mathrm{out}}$ are straightforward to derive and are not given here. Note that the maximal shear stress is now a function of the load $t$ and can grow unboundedly with it at least until $r_q$ reaches the outer boundary.

To close the problem and to determine $r_q$, we write, using the Legendre transform, the minimization problem (13) as

$$\min_{p\in\mathscr{P},p\geq 0}\ \max_{\xi\in L^2}\int_{r_1}^{r_2} 2r\left((\tau_Y - \tau)\,p + \xi\left(p' + 2\,\frac{p}{r}\right) - \frac{\xi^2}{2\mu a^2}\right)\mathrm{d}r, \tag{29}$$

introducing the dual variable $\xi$, which physically means the micro-stress associated to the plastic incompatibilities. Maximality of (29) in $\xi$ yields the constitutive equation for the *micro-stress*

$$\xi(r) = \mu a^2\left(p'(r) + 2\,\frac{p(r)}{r}\right); \tag{30}$$

minimality of (29) with respect to $p$ yields the condition

$$\tau_Y - \tau(r) = \frac{r}{2}\left(\frac{\xi(r)}{r}\right)', \tag{31}$$

in the region $[r_1, r_q)$ where plastic strain are non-vanishing. In the region $[r_q, r_2]$, where $p \equiv 0$, the constitutive Eq. (30) implies $\xi \equiv 0$. Since the source terms in (31) are $C^\infty([r_1, r_2])$, the dual field must be continuous at the interface, leading to

$$\xi(r_q) = 0 \quad \Rightarrow \quad p'(r_q) = 0. \tag{32}$$

Using (27), this variational condition translates into the following transcendental equation:

$$2\,r_q^2\,\log\frac{r_q}{r_1} = \frac{\tau_m}{\tau_Y}\left(r_q^2 - r_1^2\right), \tag{33}$$

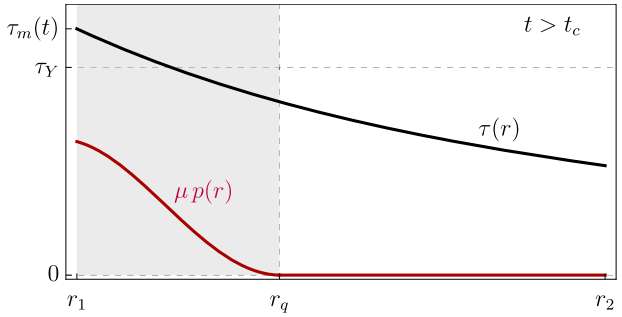


**Fig. 2.** Qualitative plot of the shear stress (black) and plastic strain (red) distributions for $t > t_c$. Note that, due to the non-local character of the yield condition, in the (gray) plastic region $[r_1, r_q]$ there are points where $\tau > \tau_Y$ and others where $\tau < \tau_Y$.

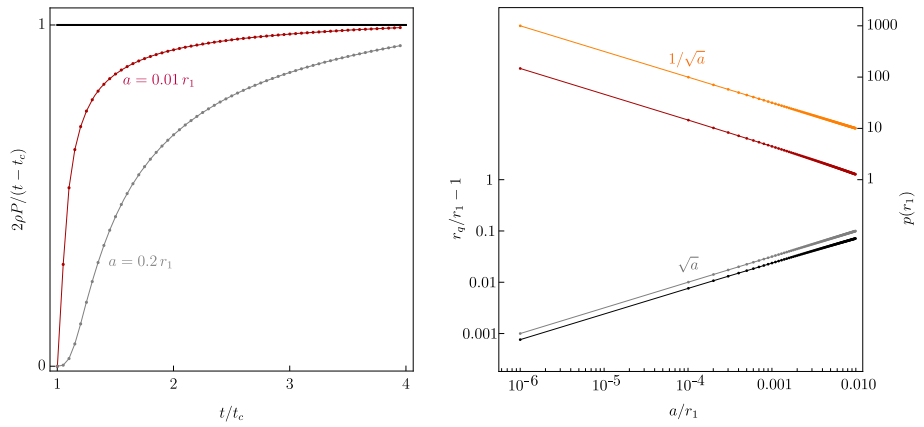


**Fig. 3.** As $a \to 0$: (Left) convergence to the perfect plasticity solution (25). In this plot, we assumed $r_2 = 2r_1$ and $t = 1.3\, t_c$; (Right) scaling of the maximal plastic strain (red points) and the size of the plastic region (black points);

which, together with (28), allows to determine $r_q$ as a function of the load $t$. Once obtained $r_q$, substitution into (27) and (28) allows to obtain the plastic strain $p(r)$ and the maximal stress $\tau_m$ as functions of the load.

The solution of (28) and (33) for $r_q$ requires root finding techniques. We point out that it is always possible to find a solution similar to the one shown in Fig. 2 where $r_q > r_1$ and $\tau_m > \tau_Y$ for $t \geq t_c$. However, note that as the load increases the size of the plastic zone also increases; our analysis is valid until $r_q \leq r_2$; this condition is satisfied for a load

$$\frac{t}{t_c} \leq \frac{\left(\rho^2-3\right)\left(\rho^2-1\right)^2 - 4\left(\rho^2-1\right)\left(\rho^2-2(a/r_1)^2\right)\log\rho + 16\rho^2\log^2\rho}{4(a/r_1)^2\left(\rho^2-1\right)^2/\rho^2}. \tag{34}$$

For $\rho = r_2/r_1 = 2$ and $a/r_1 = 0.1$ this means $t_c \leq t \leq 73.8\, t_c$. Within this range (34), the maximal stress grows monotonically with $t$ without bounds. Moreover, we can numerically prove that in the limit $a \to 0$ the area below the plastic strain graph with $p(r,t)$ in (27) tends to the amplitude of the Dirac delta $P(t)$ in (25)

$$\int_{r_1}^{r_q} p(r)\, \mathrm{d}r \to P, \tag{35}$$

for any $t$, as expected. Indeed, for $a \to 0$, we get $r_q - r_1 = O(\sqrt{a})$, whilst the maximal plastic strain $p(r_1)$ scales as $O(1/\sqrt{a})$, cfr. the numerical evidence in Fig. 3.

**Remark 5.** The condition $p'(r_q) = 0$ can also be derived by a direct variational argument. Since the plastic support $[r_1, r_q]$ is itself a free parameter of the minimization, one may require stationarity of the total energy (13) with respect to $r_q$. Applying the Leibniz rule to differentiate the integrals with variable limits, and using the fact that the fields $v$ and $p$ satisfy the Euler–Lagrange equations within each subdomain, the stationarity condition reduces to a transmission condition at the interface $r = r_q$. Since $p(r_q) = 0$ and the displacement gradient $v'$ and the shear stress $\tau$ are continuous at $r_q$, the only surviving term involves the gradient energy density evaluated at the interface. Specifically, the condition becomes

$$-\frac{1}{2}\mu a^2 r_q \left(p'(r_q)\right)^2 = 0,$$

which immediately yields $p'(r_q) = 0$.

## 6. Solution to the 1D problem: gradient plasticity with rank-one defect energy

Finally, we consider the same loading problem for the functional (14). As discussed earlier, a rank-one cost for the plastic incompatibilities allows the plastic strain to jump, $p \in \mathscr{P} = BV$, while still permitting a continuous displacement field, $v \in H^1$.

Again, the elastic phase is identical to the one described in the perfect plasticity case, but the critical load at which plastic strains appear is now higher than $t_c$. Indeed, the directional derivative of the quadratic defect energy vanishes when evaluated at $p = 0$ and, hence, does not affect the yield criterion. Instead, the rank-one defect energy we are now considering has a positive directional derivative even at $p = 0$; thus, an additional energetic cost is required for the evolution of plastic strains.

### 6.1. Dual formulation for the rank-one defect energy

We examine the implications of the minimality of the functional (14) with respect to the plastic strain field $p$

$$\min_{p\in\mathscr{P}} \hat{\mathscr{E}}_i^{\mathrm{gp1}}(p) = \int_{r_1}^{r_2} 2r\left(\tau_Y\,|p| - \tau\, p + \frac{\mu\ell}{2}\left|2\,\frac{p}{r} + p'\right|\right)\mathrm{d}r, \tag{36}$$

where $\tau(r)$ is the shear stress in (17). We focus on the onset of plasticity for $p \geq p_i = 0$; note that the non-negativity of the plastic strain is assumed for simplicity without loss of generality. Reverting the load $t$ one has a non-positive plastic strain instead.

To tackle this problem, we first consider the change of variable

$$\psi(r) := r^2 p(r), \quad \text{such that} \quad \frac{\psi'(r)}{r^2} = 2\,\frac{p(r)}{r} + p'(r).$$

Clearly $\psi \in BV$, and since in our domain $r$ is always positive, $\psi$ has the same sign as $p$, meaning $\psi \geq 0$, while $\psi'$ has no definite sign. Hence (36) is equivalent to

$$\min_{\psi \in \mathscr{P},\, \psi \geq 0} \int_{r_1}^{r_2} \left( \frac{\tau_Y\, \psi - \tau\, \psi + \mu \ell\, |\psi'|/2}{r} \right) \mathrm{d}r \tag{37}$$

where we used $p \geq 0$ to substitute $\psi$ with $|\psi|$. However, standard localization arguments do not apply to this functional due to the presence of terms containing $|\tilde{\psi}'|$ in its variation. To avoid these difficulties, owing to the convexity of the functional (37) with respect to $\psi'$, we use the dual representation of the total variation to transform the variational problem (37) into the equivalent

$$\min_{\psi \in \mathscr{P},\, \psi \geq 0} \max_{\zeta \in L^\infty, |\zeta| \leq 1} \int_{r_1}^{r_2} \left( \frac{\tau_Y\, \psi - \tau\, \psi + \mu \ell\, \zeta\, \psi'/2}{r} \right) \mathrm{d}r \tag{38}$$

where the dual field $\zeta$ is bounded ($-1 \leq \zeta \leq 1$) and has the physical meaning of a micro-stress. We proceed to solve this variational problem instead of (36).

A necessary condition for the maximality in (38) is

$$\frac{\mu \ell}{2} \int_{r_1}^{r_2} \left( \tilde{\zeta}\, \frac{\psi'}{r} \right) \mathrm{d}r \leq 0, \tag{39}$$

where the admissible variations $\tilde{\zeta}$ of the dual field must be non-negative when $\zeta = -1$, non-positive when $\zeta = 1$, and of arbitrary sign when $-1 < \zeta < 1$. Hence, (39) implies

$$\begin{cases} \zeta = -1, & \psi' \leq 0, \\ -1 < \zeta < 1, & \psi' = 0, \\ \zeta = 1, & \psi' \geq 0. \end{cases} \tag{40}$$

A necessary condition for the minimality in (38) is

$$\int_{r_1}^{r_2} \left[ \frac{\tau_Y - \tau}{r} - \frac{\mu \ell}{2} \left( \frac{\zeta}{r} \right)' \right] \tilde{\psi}\, \mathrm{d}r + \frac{\mu \ell}{2} \left[ \frac{\zeta \tilde{\psi}}{r} \right]_{r_1}^{r_2} \geq 0. \tag{41}$$

Let $\Omega_1 \subset [r_1, r_2]$ be the set of points where plasticity evolves and $\psi > 0$, while $\Omega_0$ is the set of points where plastic strain vanishes and $\psi = 0$. The admissible perturbations $\tilde{\psi}$ in (41) can have arbitrary sign in $\Omega_1$ but must be non-negative in $\Omega_0$. Therefore, with standard localization arguments in the plastic region, we get the following bulk equation for the micro-stress[2]

$$\frac{\tau_Y - \tau(r)}{r} = \frac{\mu \ell}{2} \left( \frac{\zeta(r)}{r} \right)', \quad \text{in } \Omega_1, \tag{42}$$

together with the boundary conditions $\zeta = 0$ in $r_1$ and/or $r_2$ if they belong to $\Omega_1$. In $\Omega_0$, where plasticity does not evolve, we have a differential inequality for $\zeta$:

$$\frac{\tau_Y - \tau(r)}{r} \geq \frac{\mu \ell}{2} \left( \frac{\zeta(r)}{r} \right)', \quad \text{in } \Omega_0, \tag{43}$$

with $\zeta \geq 0$ in $r_1$ and/or $r_2$ if they belong to $\Omega_0$.

Eqs. (40), (42), and (43) play the role of a *flow rule* for the rank-one model: they determine jointly the direction of plastic flow, the position of the elastic-plastic interface, and the admissibility condition in the elastic region. Crucially, this flow rule is not postulated as an independent constitutive assumption, but emerges directly as the necessary optimality conditions of the variational problem (14).

In the next two subsections we provide two analytical solutions of the above flow rule. It turns out that there exists a threshold value $\rho^c$ for the geometric ratio $\rho = r_2/r_1$ at which the solution changes dramatically: when $\rho < \rho^c$, the entire domain is subject to non-vanishing plasticity, while for $\rho \geq \rho^c$, the plastic strain localizes in an inner strip whose size depends on the characteristic length $\ell$. We do not know if other solutions are possible. Since our finite element (FE) simulations only identify the two described below (cf. Section 8), we conjecture that if other solution branches exist, they are energetically unfavorable.

[2] Although $\zeta$ is initially defined in $L^\infty([r_1, r_2])$, Eq. (42) ensures it is Lipschitz-continuous because its derivative is bounded. This regularity is critical for the integral in (38) when $\psi \in BV$. Generally, the product of a bounded function and a measure (like $p'$) is ill-defined if both jump simultaneously. However, the Anzellotti pairing (Anzellotti, 1983) provides a framework to define the functional $\langle \zeta, \psi' \rangle$, provided the dual field has a regular divergence. Here, the continuity of $\zeta$ (regularity of its divergence) eliminates ambiguity, ensuring the defect energy remains physically consistent.

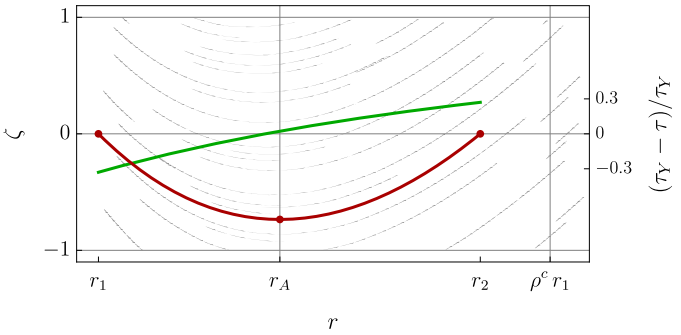


**Fig. 4.** Solution for $\zeta$ in (42) when $\rho \le \rho^c$: the red curve depicts the solution (44), the green curve shows $(\tau_Y - \tau(r))/\tau_Y$, and the gray arrows indicate the stream plot associated with (42). All these curves are obtained for $r_2 = 1.35\, r_1$, $\ell = 0.05\, r_1$, and $\tau_Y/\mu = 0.7071$.

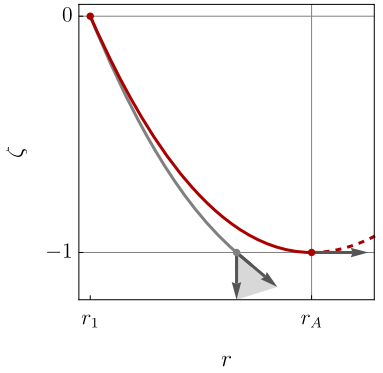


**Fig. 5.** The red curve reaches the lower bound $\zeta = -1$ with a horizontal tangent and can be continued. The gray curve reaches the lower bound with a negative slope, but the cone of admissible directions (gray) does not allow the bound to be satisfied: this is not a solution of (38).

### 6.2. *Solution A for "small" $\rho = r_2/r_1 < \rho^c$*

In this first solution plasticity evolves in the whole domain: $\Omega_1 \equiv [r_1, r_2]$. Due to the boundary conditions derived in the previous subsection, we start integrating (42) from $\zeta = 0$ in $r_1$ obtaining

$$\zeta_A(r) = \frac{2\tau_Y}{\mu\ell}\left( r \log\frac{r}{r_1} + \frac{\tau_m}{\tau_Y}\frac{r_1^2 - r^2}{2r}\right). \tag{44}$$

This function depends on the unknown value of the maximal stress $\tau_m$ in (17) which can be computed using the other boundary condition $\zeta_A(r_2) = 0$, since $r_2 \in \Omega_1$. Specifically we obtain:

$$\frac{\tau_m^A}{\tau_Y} = \frac{2\rho^2 \log\rho}{\rho^2 - 1} > 1. \tag{45}$$

The stress overshoot $\sigma_A(\rho) = \tau_m^A/\tau_Y$ is positive since $\rho > 1$ but independent of $\ell$. The function (44) has the qualitative character shown in Fig. 4: it starts from $\zeta_A(r_1) = 0$ with a negative slope $2(\tau_Y - \tau_m^A)/(\mu\ell)$ then it reaches a minimum in $r = r_A(\rho)$ with

$$r_A(\rho) = r_1\sqrt{\frac{\sigma_A(\rho)}{W\left(\sigma_A(\rho)\, e^{2-\sigma_A(\rho)}\right)}} = r_1\left(\frac{1+\rho}{2} + o(\rho - 1)\right),$$

where $W(\cdot)$ is the ProductLog function, i.e., the principal solution for $x$ in $y = x\, e^x$.

However, the function (44) is valid in the whole domain $[r_1, r_2]$ only if its value remains strictly within the bounds 1 and $-1$. On the other hand, the necessary conditions for minimality (42) and (43) imply at every point a cone of admissible directions for the curve $\zeta(r)$ in the $(r, \zeta)$ plane. With reference to Fig. 5, we observe that a curve reaching the lower bound with a negative slope is not a solution, since the admissible directions no longer allow the bound $\zeta = -1$ to be satisfied. The critical condition is to have the minimum value equal to the lower bound: $\zeta_A(r_A(\rho)) = -1$. Since the stress overshoot $\sigma_A$ increases and the minimum $\zeta_A(r_A)$ decreases with increasing $\rho$, the critical condition $\zeta_A(r_A(\rho)) = -1$ implies the following transcendental equation

$$(r_A(\rho^c))^2 - \sigma_A(\rho^c)\, r_1^2 = \frac{\mu\ell}{2\tau_Y}\, r_A(\rho^c), \tag{46}$$

to determine the highest ratio $\rho^c$ at which the solution (44) ceases to exist.

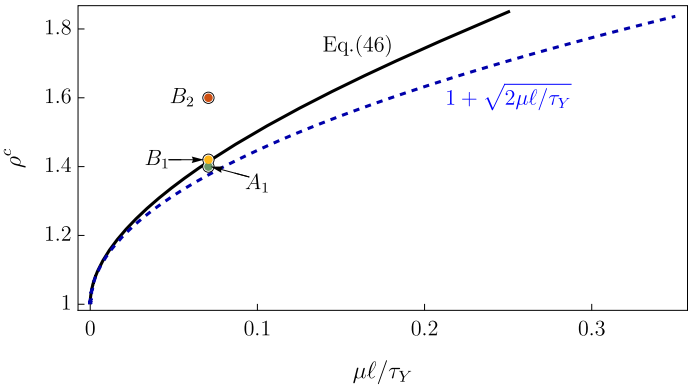


**Fig. 6.** The critical value of $\rho = r_2/r_1$ as a function of the ratio $\mu\ell/\tau_Y$: the black curve is the solution of Eq. (46), and the dashed blue curve is an approximation of this solution obtained using series expansions for $r_A(\rho)$ and $\sigma_A(\rho)$. Three points are chosen for the simulations in Section 8: $A_1$ and $B_1$ are just below and above the curve $\rho = \rho^c$, while $B_2$ is well inside the region where only solution $B$ is valid.

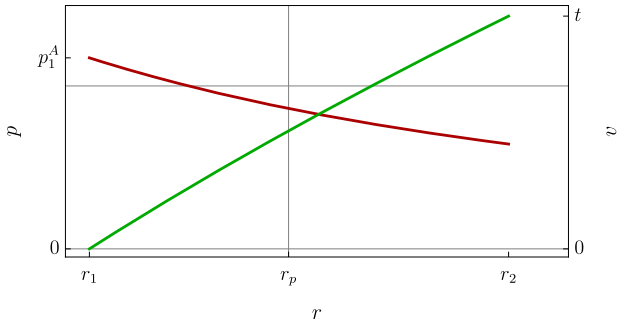


**Fig. 7.** Solutions A for the plastic strain (red, scale on the left) and the displacement (green, scale on the right) for $t = 2t_c^A$.

Once the solution for the dual variable $\zeta$ is computed, we can determine the plastic strain and the displacement. Indeed, since $\zeta_A(r)$ is strictly within the bounds for $\rho < \rho^c$, Eq. (40) dictates $\psi'(r) = 2p(r)\,r + r^2 p'(r) = 0$, meaning the curl of the plastic strain must vanish everywhere. Solving this differential equation, we obtain $p_A(r) = p_1^A r_1^2/r^2$, determining the plastic strain up to the non-negative constant $p_1^A$. Integrating the constitutive relation $v' - v/r = \tau(r)/\mu + 2p(r)$ and using the two boundary conditions $v(r_1) = 0$ and $v(r_2) = t$, we determine

$$p_1^A = \frac{\rho\,(t - t_c^A)}{\rho^2 - 1}, \quad v_A(r) = \frac{\rho\big(r^2/r_1^2 - 1\big)t}{\big(\rho^2 - 1\big)r/r_1}, \quad t_c^A := r_1\,\frac{\tau_Y}{\mu}\,\rho\log\rho. \tag{47}$$

The condition for $p_1^A$ to be non-negative, namely $t \geq t_c^A$, assigns $t_c^A$ the physical meaning of the critical load. Note that this critical load is higher than that of perfect plasticity (cf. Eq. (21)) since $t_c^A/t_c = 2\rho^2\log\rho/(\rho^2 - 1) > 1$ for $\rho > 1$. The solutions for $p$ and $v$ are plotted in Fig. 7 for $t = 2t_c^A$.

### 6.3. Solution B for "large" $\rho = r_2/r_1 \geq \rho^c$

Driven by the monotonically decreasing character of the shear stress, plasticity now evolves only in the inner part of the domain: specifically in $\Omega_1 = [r_1, r_p)$ plastic strains are positive, whilst in $\Omega_0 = [r_p, r_2]$ no plastic strain is present. Clearly the limit point $r_p$ must be determined; while, in general, it could be load-dependent, as found for $r_q$ in (33), it will be independent of the load.

Again, since $r_1 \in \Omega_1$, we start integrating (42) from the boundary condition $\zeta(r_1) = 0$ obtaining

$$\zeta_B(r) = \frac{2\tau_Y}{\mu\ell}\left(r\log\frac{r}{r_1} + \frac{\tau_m}{\tau_Y}\,\frac{r_1^2 - r^2}{2r}\right). \tag{48}$$

Again, this function depends on the unknown maximizing stress $\tau_m$, but now $\tau_m$ cannot be determined using the boundary condition at $r_2$ because we only know that $\zeta(r_2) \geq 0$, given $r_2 \in \Omega_0$. However, regardless of the value of $\tau_m$, there exists a neighborhood of $r_1$ where $-1 < \zeta < 1$. Within this neighborhood, (40) dictates that the plastic strain must have a vanishing curl, $\psi' = 0$, yielding the form $p(r) = p_1^B r_1^2/r^2$ with $p_1^B$ a positive constant (the case $p_1^B = 0$ is the trivial elastic phase). Since this field is strictly positive for any finite $r$, the existence of a purely elastic region $\Omega_0$ where $p = 0$ necessitates a jump discontinuity in the plastic strain. Specifically, there must exist a point, say $r_p$, where $\psi' < 0$ and the plasticity vanishes abruptly. By virtue of (40), this in turn implies that the function

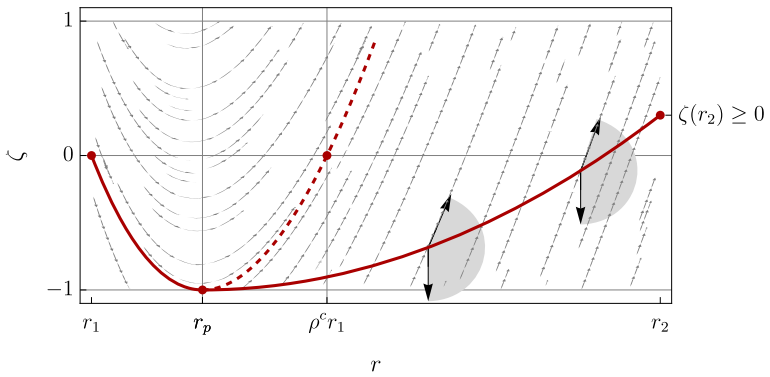


**Fig. 8.** Solution for $\zeta$ in (42) when $\rho \geq \rho^c$ (solid red curve). For $r \leq r_p$, the solution is (48) dictated by (42); for $r \geq r_p$, we have plotted only one possible solution satisfying the differential inequality (43) and the boundary condition $\zeta(r_2) \geq 0$. The dashed red curve indicates another possible solution that satisfies (42) for $r > r_p$. All these curves are obtained for $\rho = 2$ and $\mu\ell/\tau_Y = 0.071\, r_1$.

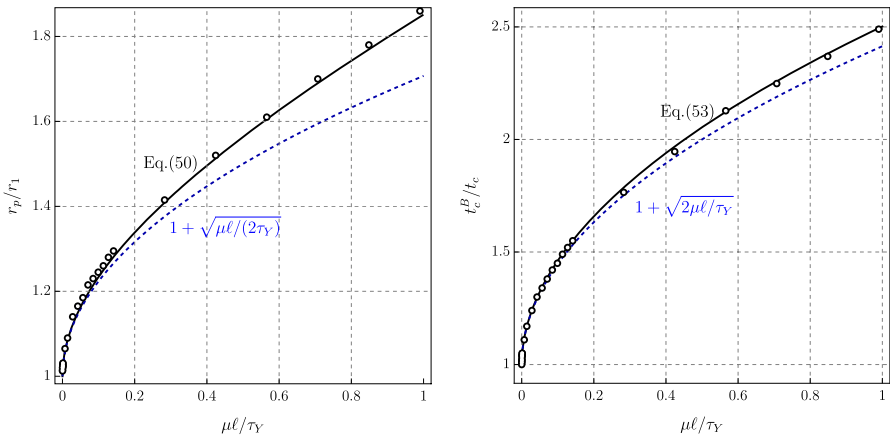


**Fig. 9.** Left: the limit point for the plastic zone as a function of the ratio $\mu\ell/\tau_Y$. Right: the critical load (53) as a function of the ratio $\mu\ell/\tau_Y$. The points report the numerical results found by the Finite Element code described in Section 8. Both these plots assume a value for $r_2$ higher than the critical $\rho^c$ evaluated at $\mu\ell/\tau_Y = 1$.

$\zeta$ reaches its lower bound with a horizontal tangent (see the discussion pertaining to Fig. 5). Consequently, the parameters $\tau_m$ and $r_p$ are uniquely determined by the conditions $\zeta_B(r_p) = -1$ and $\zeta_B'(r_p) = 0$; specifically using (48) we get the stress overshoot as a function of $r_p$

$$\frac{\tau_m^B}{\tau_Y} = \frac{r_p\left(\mu\ell/\tau_Y + 2\, r_p \log(r_p/r_1)\right)}{r_p^2 - r_1^2}, \tag{49}$$

and a transcendental equation to determine the limit point $r_p$

$$4\, r_1^2 r_p \log\frac{r_p}{r_1} + \frac{\mu\ell}{\tau_Y}\left(r_p^2 + r_1^2\right) = 2 r_p\left(r_p^2 - r_1^2\right), \tag{50}$$

which, as anticipated, turns out to be independent of the load $t$ and depends only on the ratio $\mu\ell/\tau_Y$.

Beyond the point $r_p$, plastic strains vanish, and $\zeta$ must only satisfy the differential inequality (43) and the boundary condition $\zeta(r_2) \geq 0$. A possible solution is shown in Fig. 8, where we have plotted the streamlines induced by (42) and, at some points, the cone of admissible directions dictated by (43). Clearly, if $r_2 < \rho^c r_1$, there is not enough space for $\zeta$ to reach non-negativity at $r_2$; this solution is no longer valid, and we revert to Case A of the previous section. However, in the interval $[r_p, r_2]$, any other curve $\zeta(r)$ satisfying (43) and reaching a non-negative value at $r_2$ is a solution of (38). Note that hitting the upper bound and remaining at $\zeta = 1$ is also an admissible solution.

The solution to (50) can be found numerically to an arbitrary precision and it is plotted in Fig. 9 against the parameter $\mu\ell/\tau_Y$. Note that the support of plastic strain $[r_1, r_p]$ grows as $\sqrt{\ell}$ for small characteristic lengths.

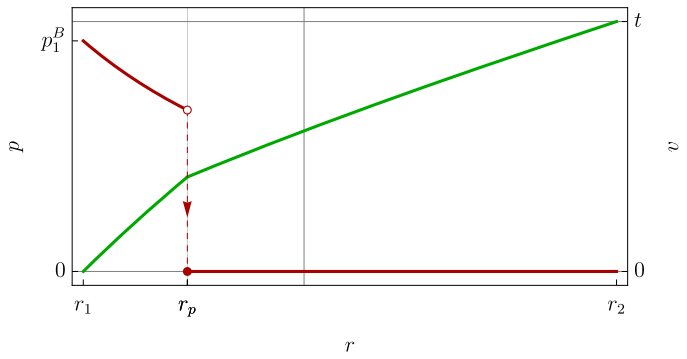


**Fig. 10.** Solutions B for the plastic strain (red) and the displacement (green) for $t = 2t_c^B$.

As before, once the dual function $\zeta$ is determined, we can compute the plastic strain and the displacements. This is done by splitting the solution of the constitutive relation into the two domains

$$\begin{cases} v'_{\text{in}} - \dfrac{v_{\text{in}}}{r} = \left(\dfrac{\tau_m^B}{\mu} + 2\,p_1^B\right)\dfrac{r_1^2}{r^2}, & \text{for } r_1 \le r \le r_p \\ v'_{\text{out}} - \dfrac{v_{\text{out}}}{r} = \left(\dfrac{\tau_m^B}{\mu}\right)\dfrac{r_1^2}{r^2}, & \text{for } r_p \le r \le r_2 \end{cases} \tag{51}$$

and using the two boundary conditions $v_{\text{in}}(r_1) = 0$ and $v_{\text{out}}(r_2) = t$ and the continuity of the displacement $v_{\text{in}}(r_p) = v_{\text{out}}(r_p)$ to determine the plastic strain at the inner boundary

$$p_1^B = \frac{\mu r_p^2\left(2r_2 t\left(r_p^2 - r_1^2\right) + \left(r_1^2 - r_2^2\right)\ell r_p\right) + 2\left(r_1^2 - r_2^2\right)r_p^4\tau_Y \log(r_p/r_1)}{2\mu r_2^2\left(r_1^2 - r_p^2\right)^2}. \tag{52}$$

Imposing the non-negativity of $p_1^B$ we determine the critical load

$$t_c^B = \frac{2r_p \log\left(r_p/r_1\right) + \mu\ell/\tau_Y}{\left(r_p^2 - r_1^2\right)/r_p}\, t_c. \tag{53}$$

Again, note that since $r_p \ge r_1$, we have $t_c^B/t_c \ge 1$; therefore, the critical load $t_c^B$ obtained with the rank-one defect energy is higher than that in perfect plasticity (21). Since $r_p = r_p(\mu\ell/\tau_Y)$ by (50), in Fig. 9 Right we have plotted $t_c^B/t_c$ as a function of the ratio $\mu\ell/\tau_Y$ and have provided its series expansion near $\mu\ell/\tau_Y = 0$. The qualitative solutions for $p$ and $v$ are plotted in Fig. 10 for $t > t_c^B$. Note that $v$ is continuous but its derivative jumps at $r = r_p$, where the curl of the plastic strain is localized as a Dirac distribution $\delta(r - r_p)$ (see Table 1). Indeed, $\operatorname{curl}\mathbf{E}^{\text{p}}$ vanishes identically both for $r < r_p$ and for $r > r_p$, and all the plastic incompatibility is concentrated at the front $r = r_p$. Note that, while $r_p$ is independent of the load $t$, $p_1^B$ grows with $t$, as do the jumps in the plastic strain and the displacement derivative.

As noted for the solution of the quadratic defect energy in Fig. 3, the perfect plasticity solution (25) with the Dirac delta at $r = r_1$ can be recovered in the limit as $\ell \to 0$. Indeed, from (50) and (52), it can be shown that $r_p - r_1 = O(\sqrt{\ell})$ and $p_1^B = O(1/\sqrt{\ell})$.

**Remark 6.** An alternative approach to the solution described above could have been the following. We assume for the plastic strain the Ansatz

$$p(r) = \begin{cases} p_1^B (r_1/r)^2 & r_1 \le r < r_p \\ 0 & r_p \le r \le r_2 \end{cases}. \tag{54}$$

We determine the associated inner/outer displacement fields via the constitutive equation and the maximal stress $\tau_m$ via the continuity of the displacement in $r_p$. With these solutions for $p$ and $v$, we set up a reduced energy functional

$$\mathscr{G}_t(p_1^B, r_p) = \frac{\mu r_1\left(p_1^B r_2\left(r_p^2 - r_1^2\right) - t\, r_p^2\right)^2}{r_p^4\left(r_1^2 - r_2^2\right)} + 2\,\tau_Y\, p_1^B r_1^2 \log\frac{r_p}{r_1} + \mu\ell\, p_1^B\,\frac{r_1^2}{r_p}, \tag{55}$$

where the three terms (resp. elastic energy, plastic dissipation, and defect energy) depend only on two degrees of freedom: $p_1^B$ and $r_p$. The stationarity conditions for $\mathscr{G}_t$ with respect to $p_1^B$ and $r_p$ are

$$\frac{\partial \mathscr{G}_t}{\partial p_1^B} = 0, \qquad \frac{\partial \mathscr{G}_t}{\partial r_p} = 0. \tag{56}$$

**Table 1**
Comparative summary of the main analytical results for perfect plasticity (p), quadratic gradient plasticity (gp2), and one-homogeneous gradient plasticity (gp1); the latter has two regimes depending on the ratio $\rho$. The table highlights differences in critical load, maximal stress overshoot, plastic support, and regularity of the curl of the plastic strains.

| Model | | Critical load | Maximal stress | Plastic support | Curl $\mathbf{E}^p$ |
|---|---|---|---|---|---|
| p | | $t_c$ | $\lvert\tau\rvert < \tau_Y$ | $\{r_1\}$ | – |
| gp2 | | $t_c$ | unbounded and depending on $t, \alpha, \rho$ Eq. (28) | $[r_1, r_q(t,\alpha,\rho)]$ Eq. (33) | $\in H^1([r_1, r_2])$ |
| gp1 | **A** $\rho < \rho^c(\ell)$ | $f_A(\rho)\cdot t_c$ Eq. (47) | $\lvert\tau\rvert < \tau_m(\rho)$ Eq. (45) | $[r_1, r_2]$ | 0 |
| | **B** $\rho \geq \rho^c(\ell)$ | $f_B(\lambda)\cdot t_c$ Eq. (53) | $\lvert\tau\rvert < \tau_m(\lambda)$ Eq. (49) | $[r_1, r_p(\lambda)]$ Eq. (50) | $\delta(r - r_p)$ |

Eliminating the load $t$ from these two we get

$$\left[4\, r_1^2 r_p \log\frac{r_p}{r_1} + \frac{\mu\ell}{\tau_Y}\left(r_p^2 + r_1^2\right) - 2r_p\left(r_p^2 - r_1^2\right)\right] p_1^B = 0, \tag{57}$$

meaning that either $p_1^B = 0$ (the elastic phase) or the transcendental Eq. (50) to determine $r_p$ must hold. From $(56)_1$ we get exactly (52). The convexity of $\mathscr{G}_t$ with respect to its arguments can be checked numerically on the solution branch. The merit of our previous derivation is to prove that (54) is not merely an Ansatz, but an exact solution of the variational problem (14).

**Remark 7.** The optimality conditions (40)–(43) are rooted in the same mechanical framework developed in Forest and Guéninchault (2013), Wulfinghoff et al. (2015): the dislocation density tensor $\operatorname{curl}\mathbf{E}^p$ enters the free energy, and the rank-one energy gives rise to a stress-like field conjugate to $\operatorname{curl}\mathbf{E}^p$ that is bounded in norm - the tensor counterpart of our micro-stress field $\zeta$. In this sense, the present model belongs to the same family of gradient plasticity theories. The key distinction concerns the treatment of the plastic support. In Forest and Guéninchault (2013), Wulfinghoff et al. (2015), the geometry of the laminate prescribes the support of plastic slip from the outset, and a generalized yield criterion is postulated separately to close the system. In the present work, no a priori assumption on the support is made: the conditions (40)–(43) emerge entirely from the minimization of the incremental potential (14), and simultaneously determine the plastic field within the active zone and the location of its boundary. The variational framework thus replaces the postulated yield criterion with optimality conditions that include, as an essential ingredient, the inequality (43) and the associated boundary conditions, sealing the inactive zone.

## 7. Comparative overview: quadratic vs. rank-one gradient plasticity

In this section, we provide a comprehensive comparative overview of the results obtained using the three models discussed: classical von Mises perfect plasticity (p), and gradient plasticity endowed with either quadratic (gp2) or rank-one (gp1) defect energy. The main analytical features of these models are summarized in Table 1, highlighting how the specific choice of regularization fundamentally alters the mechanisms of plastic nucleation and the subsequent evolution of the plastic strain field. We observe that, together with the external load parameter $t$, the overall mechanical scenario is governed by three dimensionless parameters:

$$\rho = \frac{r_2}{r_1}, \quad \alpha = \frac{\mu\, a}{\tau_Y r_1}, \quad \lambda = \frac{\mu\,\ell}{\tau_Y r_1}, \tag{58}$$

representing respectively the geometry of the annular domain and the constitutive internal length scales associated with the two distinct regularizations.

The first critical difference lies in the critical load required for the onset of plasticity. In both the classical perfect plasticity and the quadratic defect energy models, yielding remains a strictly local event that initiates at a critical threshold $t_c$, regardless of the internal length scale $a$. In sharp contrast, the rank-one model predicts a genuine *strengthening* effect: the yield threshold is shifted to a strictly higher value ($t_c^A$ or $t_c^B$, depending on the selected geometric regime). This threshold elevation reflects the presence of a discrete energetic barrier that must be overcome to activate a structured plastic zone.

This nonlocal strengthening phenomenon physically manifests as a *stress overshoot* ($|\tau_m|/\tau_Y > 1$), a feature strictly forbidden in classical plasticity where $|\tau| \leq \tau_Y$ is always enforced. In the rank-one gradient setting, the elastic stress is permitted to safely exceed the local yield limit because of the emergence of a *back-stress* $\tau_{\text{back}}$, generated by the distribution of GNDs representing the lattice incompatibility. Mathematically, the dual field $\zeta$ embodies this back-stress: its distributional derivative acts as a distributed "gradient

resistance." Rewriting the established balance Eq. (42) as

$$\tau(r) = \tau_Y - \underbrace{\frac{\mu\ell}{2}\, r\left(\frac{\zeta(r)}{r}\right)'}_{\tau_{\text{back}}}, \tag{59}$$

we clearly see how this back-stress counteracts the surplus mechanical driving force, preventing the activation of further plastic slip even when the elastic stress exceeds the typical local bounds.

Moreover, a crucial distinction exists regarding how this stress overshoot evolves with the applied load. In the quadratic model (gp2), the maximal stress is unbounded and depends on the load parameter $t$ as the plastic front gradually sweeps through the domain. By contrast, in the rank-one model (gp1), the maximal stress is bounded and load-independent; in this respect, gp1 maintains a characteristic, and sometimes useful, feature of perfect plasticity. This distinctive behavior is a direct consequence of the stationary geometry of the plastic support: once the minimum energy nucleation regime has been established, the plastic front is locked, the back-stress profile remains fixed in space. Thus, any increase in the prescribed external load $t$ must be entirely accommodated by a proportional intensification of the localized GND wall-and a corresponding increase in the plastic slip jump-rather than a gradual spatial expansion of the plastic zone.

The size of the plastic support represents another profound discriminator among the theories. Classical perfect plasticity forces the deformation into a localized point-singularity at the inner boundary $r = r_1$. The quadratic gradient model (gp2) naturally regularizes this singularity by distributing the plastic strain over a continuous, smoothly expanding support interval $[r_1, r_q(t)]$. Conversely, the rank-one gradient model (gp1) determines the spatial support at the very moment of nucleation, sorting the behavior into two distinct geometric modes:

- *Case A ($r_2/r_1 < \rho^c(\ell)$):* Plasticity unconditionally erupts over the entire annulus $[r_1, r_2]$. The system deliberately circumvents the energetic penalty associated with localized dislocation pile-ups by selecting a completely compatible, curl-free plastic flow. In this state, the required back-stress remains strictly within its bounds ($|\zeta| < 1$). Consequently, the overall macroscopic response-such as the critical load and overshoot magnitude-shows little overt dependence on the internal length $\ell$. Instead, $\ell$ serves as a subtle *topological selector*, checking only whether this compatible regime represents an admissible global minimum.
- *Case B ($r_2/r_1 \geq \rho^c(\ell)$):* The globally compatible solution ceases to be mathematically admissible because attempting to sustain it would force the back-stress $\zeta$ to exceed its bounds. At this critical threshold, the structural energetics abruptly shift. It becomes highly favorable for the solid to restrict the plastic flow exclusively within a partial annular nucleus $[r_1, r_p]$. To effectively seal off the rest of the elastic domain against yielding, the system constructs a singular GND wall (representing a concentrated dislocation pile-up) exactly at the locked forward boundary $r_p$.

Within this deeply localized regime (Case B), the internal length $\ell$ plays an essential role in dictating the intrinsic spatial extent of the plastic nucleus. Balancing the concentrated geometric decay of the elastic stress field against the gradient cost of establishing the singular wall gives rise to an emergent scaling length $r_p - r_1 \sim \sqrt{(\mu\ell)/\tau_Y}$.

## 8. Numerical results and discussion

We use the analytical solutions discussed in the previous sections as a benchmark to test our dedicated numerical solver. The code is developed starting from the functionals in Section 2 under plane strain assumptions. Once validated, the same numerical framework is used to predict the solutions for more complex geometries where the polar symmetry of the circular problem is broken.

### 8.1. Numerical implementation

The problem is discretized using the finite element method. The displacement field is approximated using standard continuous quadratic Lagrange elements.

For the plastic strain $\mathbf{E}^{\mathrm{p}}$, we exploit its symmetric and deviatoric structure. Assuming plastic incompressibility in the present two-dimensional setting, the plastic strain tensor is completely determined by two independent components, say $p$ and $q$, such that $\mathbf{E}^{\mathrm{p}}_{11} = -\mathbf{E}^{\mathrm{p}}_{22} = q$ and $\mathbf{E}^{\mathrm{p}}_{12} = \mathbf{E}^{\mathrm{p}}_{21} = p$.

A finite defect energy in (4) requires $\mathbf{E}^{\mathrm{p}}$ to belong to the space $H(\mathrm{curl})$ of tensor fields having square-integrable curl components. In the discrete setting, a tensor field satisfies $\mathbf{E}^{\mathrm{p}} \in H(\mathrm{curl})$ if its tangential components are continuous across element interfaces. Let $\mathbf{t} = (t_x, t_y)^T$ be the unit tangent vector along an edge. The tangential component of the plastic strain tensor is the vector:

$$\mathbf{E}^{\mathrm{p}}\,\mathbf{t} = \begin{pmatrix} q & p \\ p & -q \end{pmatrix}\begin{pmatrix} t_x \\ t_y \end{pmatrix} = \begin{pmatrix} t_x & t_y \\ -t_y & t_x \end{pmatrix}\begin{pmatrix} q \\ p \end{pmatrix} = \mathbf{R}(\mathbf{t})\mathbf{w}, \tag{60}$$

where $\mathbf{w} = (q, p)^T$ and $\mathbf{R}(\mathbf{t})$ is a rotation matrix map with unit determinant. Since $\mathbf{R}(\mathbf{t})$ is invertible, the tangential continuity of $\mathbf{E}^{\mathrm{p}}$ is mathematically equivalent to the full $C^0$ continuity of the associated vector $\mathbf{w}$. This key property circumvents the need for complex Nédélec-type elements and allows the discrete approximation of the independent variables of $\mathbf{E}^{\mathrm{p}}$ to be straightforwardly achieved using standard continuous linear Lagrange ($P_1$) elements.

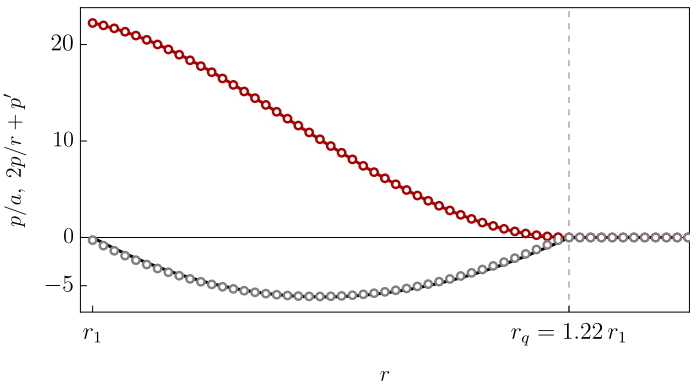


**Fig. 11.** Comparison between analytical solutions (continuous curves) and numerical results (circles) for the quadratic defect energy. In red and gray we plot respectively the plastic strain divided by the characteristic length $p/a$, see (27), and its curl $(2p/r + p')$ as functions of $r$. Here $\rho = 2$, $t = 2\, t_c$ and $\alpha = 0.071$.

Consistent with this parameterization, the two independent components of the curl of the tensor field $\mathbf{E}^{\mathrm{p}}$ can be listed in the vector:

$$\operatorname{curl} \mathbf{E}^{\mathrm{p}} \sim \begin{pmatrix} \partial_x p - \partial_y q \\ -\partial_x q - \partial_y p \end{pmatrix}. \tag{61}$$

In the discrete setting, we approximate the independent variables $p$ and $q$ using linear Lagrange ($P_1$) basis functions. Since the gradients of these functions are constant over each triangular element, the discrete curl (61) is piecewise constant throughout the mesh. This discretization of the plastic strains is used to tackle both (4) and (5).

The evolution problem is solved in an incremental framework in $\mathbf{u}$ and $\mathbf{E}^{\mathrm{p}}$ until convergence at each load step. In particular, the presence of the curl terms in the defect energy implies a nonlocal character to the problem, rendering standard local return-mapping algorithms inapplicable. Furthermore, the rank-one terms—namely, the plastic dissipation and the `gp1` defect energy—introduce non-smoothness that makes standard differential approaches like the Newton-Raphson method inefficient.

To address these numerical challenges, we recast the incremental minimization as a conic optimization problem. Following the approach detailed in Bleyer (2022), each segment of the energy functional can be rewritten using linear objectives and second-order (or rotated second-order) conic constraints via an epigraph representation. The resulting large-scale conic problem is then effectively solved utilizing the interior-point optimizer MOSEK (The MOSEK optimizer API for Python, 2019), integrated within the FEniCSx environment (Baratta et al., 2023) by means of the `dolfinix_optim` package. Interior-point methods prove particularly robust for this class of non-smooth optimization problems, guaranteeing stable and accurate solutions even in regions characterized by sharp transitions or highly localized plastic fronts. A sample code for the numerical solution of the proposed problems can be found in the repository http://github.com/a-rodella/r1-gradient-plasticity-nucleation.

### 8.2. Validation against the analytical solutions

Fig. 11 compares the benchmark solution obtained in Section 5 for the quadratic defect energy with the corresponding Finite Element results. In particular, for $\rho = 2$, $t = 2\, t_c$ and $\alpha = 0.071$, we compare the plastic strain distribution $p$ given in (27) and its curl, $(2p/r + p')$. The agreement with the numerical results is excellent. Moreover, we show that the function $2p/r + p'$, although only required to be square-integrable, is in fact more regular in the present case and belongs to $H^1 \subset L^2$, as anticipated in Table 1.

Assuming $\mu\ell/\tau_Y = 0.071\, r_1$, Fig. 12 compares the analytical and numerical solutions for the rank-one model at three values of $\rho$ marked in Fig. 6: $\rho \in \{1.4, 1.42, 1.6\}$; note that the critical transition between regime A and B occurs at $\rho^c = 1.41$. The applied load is $t = 2\, t_c$ for all cases. The left panel shows the plastic strain $p$: in regime A ($A_1$), plasticity spreads over the entire domain, whereas in regime B ($B_1$, $B_2$), it is supported on $[r_1, r_p]$ and drops to zero at the locked front $r_p = 1.19\, r_1$. The front position $r_p$ is determined solely by $\mu\ell/\tau_Y$ via Eq. (50), consistently for both $B_1$ and $B_2$. The displacement field $v$ (right panel) remains continuous everywhere, in stark contrast to the perfect plasticity solution (gray curve), where the deformation concentrates at $r = r_1$ producing a displacement jump. Across all tested configurations, the finite element results (circles) perfectly match the continuous analytical curves.

### 8.3. Response under non-proportional loading

While the analytical solutions are restricted to monotonic loading, the incremental variational framework naturally accommodates arbitrary loading paths. A complete loading–unloading–reloading cycle is tested to investigate the system's response to load reversal, particularly to verify the absence of the spurious elastic-gap phenomenon observed in non-incremental SGP theories (Panteghini et al., 2019; Nielsen and Hutchinson, 2021). We note that, as shown in (Fleck and Willis, 2015), incremental formulations are not immune to this phenomenon when non-local terms appear in the dissipation potential; in the present model, no such gradient dissipation is present.

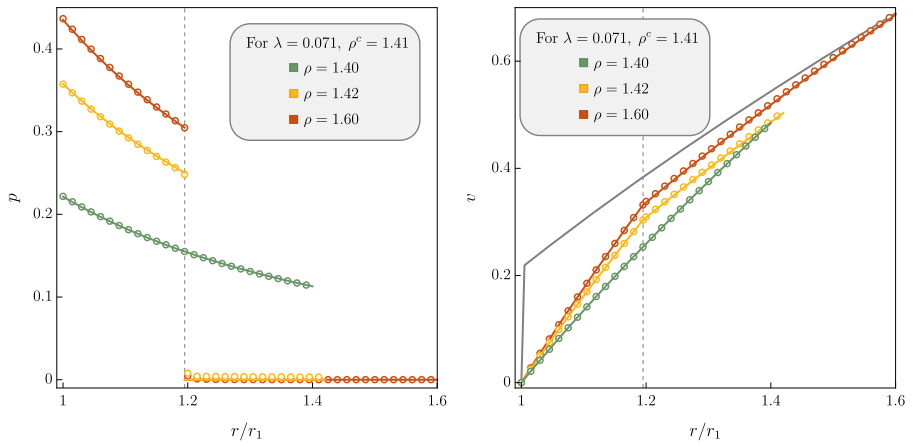


**Fig. 12.** Comparison of analytical (solid curves) and numerical (circles) profiles for the rank-one model ($\lambda = 0.071, t = 2\,t_c$) at three geometric ratios: $\rho = 1.4$ (green, regime A), $\rho = 1.42$ (yellow, regime B), and $\rho = 1.6$ (red, regime B). (*Left*) Plastic strain $p(r/r_1)$. (*Right*) Cumulative displacement $v(r/r_1)$, compared with the singular perfect plasticity solution for $\rho = 1.6$ (gray curve).

Fig. 13 illustrates the global torque response (left) and the evolution of the plastic strain $p(r_1)$ (right) against the imposed displacement $t$. Upon load reversal from the perfectly plastic plateau, the system unloads elastically until yielding symmetrically at the opposite threshold. Crucially, as $p(r_1)$ returns to zero, plastic flow reactivates immediately at the correct yield threshold without an intervening elastic gap. This response confirms the thermodynamic consistency of the incremental formulation under complex loading paths and demonstrates that the predicted strengthening represents a genuine structural activation barrier.

### 8.4. Elliptic geometry

Real microstructures rarely possess exact circular symmetry. The local asymmetry of elongated voids or notch tips breaks the symmetry of the stress field, introducing directionality in the nucleation process. To explore this, we consider a domain having a circular external boundary with the same load as before, but the inner boundary is now an ellipse.

By varying the aspect ratio $\beta := r_a/r_b \in \{1, 1.3, 2, 3.5\}$, we activate the full two-dimensional geometric structure of the rank-one model, with plastic incompatibility measured by the two non-zero components in (61).

Fig. 14 reports the normalized critical load $t_c(\beta, \lambda)/t_c(\beta, 0)$ as a function of the internal length $\lambda = \mu\ell/(\tau_Y r_1)$. Fitting the numerical data with power laws of the form $1 + A\lambda^B$ reveals that the analytically derived square-root scaling ($B = 0.5$) serves as a lower bound restricted to circular geometries. For elliptical voids, the exponents consistently exceed $1/2$ and grow monotonically with $\beta$ ($B \in \{0.59, 0.64, 0.67\}$), emphasizing a strong coupling between geometric anisotropy and the energetics of nucleation.

The spatial character of the yielding is visualized in Fig. 15, which displays the cumulative plastic strain (left half) and incompatibility $|\operatorname{curl}\mathbf{E}^p|$ (right half). For the mildly elongated ellipse ($\beta = 1.3$), the incompatibility concentrates in a closed, nearly uniform layer at a finite distance from the hole contour, echoing the variationally selected inner nucleation support of the annular benchmark. However, for higher aspect ratios ($\beta = 2$ and 3.5), the plastic field rapidly changes topology: a strongly preferred nucleation site emerges at the tips of the ellipse. The incompatibility assumes the form of narrowly confined tongues radiating from the tips,

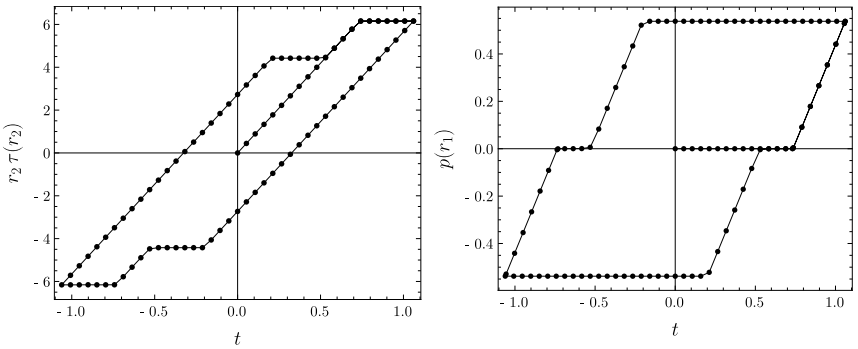


**Fig. 13.** Response under a complete loading–unloading–reloading cycle. (*Left*) Global response in terms of the torque $r_2\tau(r_2)$ at the external boundary as a function of the imposed tangential displacement $t$. (*Right*) Evolution of the plastic strain at the inner boundary, $p(r_1)$, versus $t$. In both figures, we assume $\rho = 2$ and $\lambda = 0.071$. .

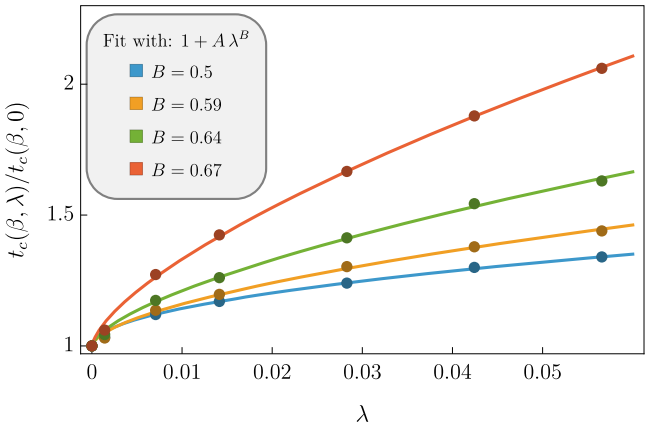


**Fig. 14.** Normalized critical load $t_c(\beta,\lambda)/t_c(\beta,0)$ as a function of the dimensionless internal length $\lambda = \mu\ell/(\tau_Y r_1)$ for the circular hole ($\beta = 1$) and three elliptical holes ($\beta \in \{1.3, 2, 3.5\}$), as indicated in the legend. Dots: numerical results. Continuous curves: power-law fits $1 + A\lambda^B$, with exponents $B \in \{0.5, 0.59, 0.64, 0.67\}$ for increasing aspect ratios.

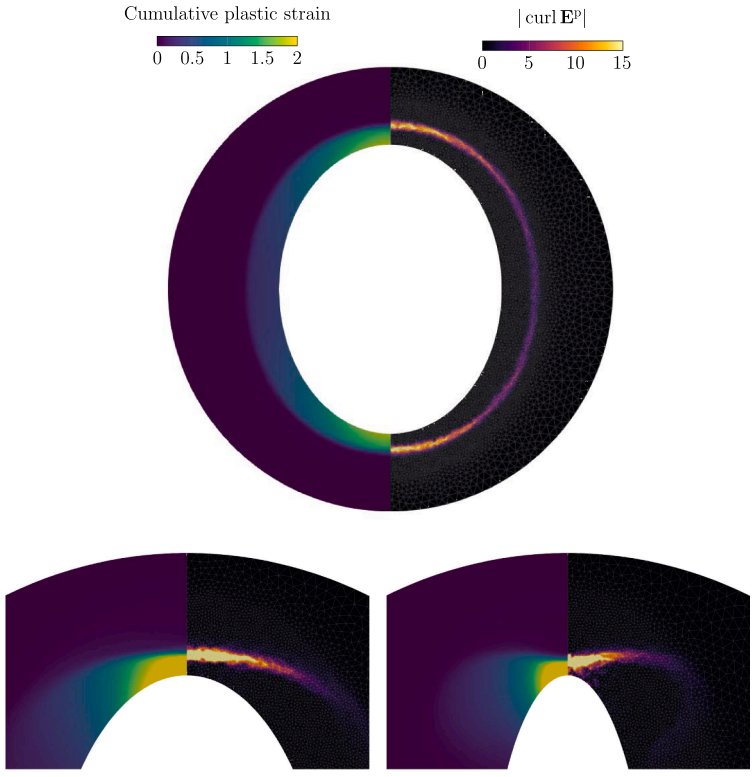


**Fig. 15.** Cumulative plastic strain (left half of each panel) and $|\operatorname{curl}\mathbf{E}^p|$ (right half) for three elliptical holes. Top: moderately elongated ellipse ($r_a/r_b = 1.3$), showing a nearly uniform closed layer of incompatibility surrounding the hole. Bottom left and right: zooms near the tip for $r_a/r_b = 2$ and $r_a/r_b = 3.5$, showing the progressive concentration of both fields at the ellipse tip and the increasingly rapid spatial decay away from it.

decaying sharply into the elastic interior. This open spatial pattern acts to balance the intense stress concentrations at the highly curved tips against the gradient penalty imposed by the rank-one energy. The more elongated the void, the steeper the concentration of the driving force and the tighter the spatial confinement of the plastic nucleus.

Fig. 16 shows the torque-displacement cycles for the three elliptical geometries and the circular case. All four cases exhibit closed, symmetric hysteresis loops with no elastic gap, confirming the incremental consistency of the formulation independently of the domain geometry. Two qualitative differences distinguish the elliptical cases from the circular one. First, the post-yield branch acquires a positive slope, reflecting a geometric hardening effect: as plastic strain accumulates at the tips, the stress redistributes and the global torque response is no longer perfectly flat. This is not a material hardening but a structural effect induced by the domain

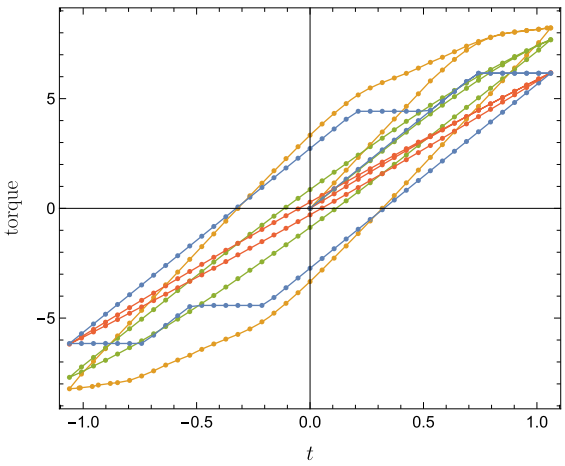


**Fig. 16.** Torque-displacement cycles for the circular hole ($\beta = 1$, blue) and three elliptical holes ($\beta = 1.3$ yellow, $\beta = 2$ green, $\beta = 3.5$ red) under a complete loading–unloading–reloading cycle.

geometry. Second, the elastic-to-plastic transition is smoother, because nucleation initiates at the tips and spreads gradually rather than occurring simultaneously along the entire contour. The resulting loop morphology — inclined branches, rounded corners, central symmetry — bears a qualitative resemblance to hysteresis loops observed experimentally in precipitation-hardened alloys (Taillard and Pineau, 1982), where similar features arise from the interplay between nucleation barriers and progressive plastic activity. While the physical mechanisms and scales differ, the analogy suggests that geometric hardening and spatially progressive nucleation are sufficient ingredients to reproduce the essential features of cyclic plastic response.

## 9. Conclusions and perspectives

The results of this work establish that, within a rank-one strain-gradient plasticity framework, the geometry of the domain is not merely a parameter but a genuine control variable of the nucleation process. Leaving the plastic support free — rather than prescribing it — is what makes this dependence visible: for the circular case, it produces two analytically tractable nucleation regimes, a square-root scaling law that is the fundamental signature of unconstrained nucleation, and a locked-front behavior with no counterpart in classical or quadratic SGP models. The exact analytical solutions derived for the annular benchmark, requiring no a priori assumptions on the plastic support, provide a rigorous foundation for the numerical investigation of more complex geometries, where the coupling between internal length and domain shape produces geometry-dependent scaling exponents that cannot be inferred from the symmetric case alone.

The present framework opens several directions for future research. A natural extension is the inclusion of crystallographic anisotropy, by replacing the isotropic rank-one term $|\operatorname{curl}\mathbf{E}^{\mathrm{p}}|$ with $|\mathbb{K}\operatorname{curl}\mathbf{E}^{\mathrm{p}}|$, where $\mathbb{K}$ is a fourth-order tensor encoding directional energetic costs. This would allow the model to distinguish between easier and harder slip directions, providing a bridge between continuum SGP and discrete dislocation dynamics.

Further developments include the inclusion of plastic spin to extend the framework to large-strain regimes, and the coupling between local dissipation and plastic strain gradients, which may reveal new length-scale effects in the post-yield evolution. Variational frameworks for such couplings have been derived via homogenization in Andrieux et al. (1996); gradient contributions to the dissipation potential have also been explored recently in Bacquaert et al. (2025) in the context of softening plasticity regularization.

## Declaration of generative AI and AI-assisted technologies in the manuscript preparation process

During the preparation of this work the authors used Gemini 3 and ChatGPT-4o in order to improve grammar and English language. After using this tool, the authors reviewed and edited the content as needed and take full responsibility for the content of the published article.

## CRediT authorship contribution statement

**Maria Chiara Comella:** Writing – review & editing, Software, Investigation, Formal analysis, Conceptualization; **Antonino Favata:** Writing – review & editing, Writing – original draft, Supervision, Investigation, Formal analysis, Conceptualization; **Andrea Rodella:** Writing – review & editing, Software, Investigation, Formal analysis, Conceptualization; **Stefano Vidoli:** Writing – review & editing, Writing – original draft, Supervision, Investigation, Formal analysis, Conceptualization.

## Data availability

No data was used for the research described in the article.

## Declaration of competing interest

The author declare that they have no known competing financial interests or personal relationships that could have appeared to influence the work reported in this paper.

## Acknowledgments

The authors thank Prof. Lorenzo Bardella and Prof. Vito Crismale for useful discussions. The authors gratefully acknowledge the support of the GNFM of the Istituto Nazionale di Alta Matematica (INdAM). The support of Sapienza University of Rome through the project “Coupling plasticity and damage for effective modeling of ductile fracture in thin structures” (CUP B83C24007070005) is also acknowledged. MCC acknowledges the support of Sapienza University of Rome through the projects “Variational approach to describe hydrogen embrittlement” (B83C24005300005) and “Hydrogen-driven Shear Band Nucleation in Anisotropic Materials through Gradient Plasticity” (B83C25004300005) .

## References

Anand, L., Gurtin, M.E., Lele, S.P., Gething, C., 2005. A one–dimensional theory of strain-gradient plasticity: formulation, analysis, numerical results. J. Mech. Phys. Solids 53 (8), 1789–1826. https://doi.org/10.1016/j.jmps.2005.03.003

Andrieux, S., Joussemet, M., Lorentz, E., 1996. A class of constitutive relations with internal variable derivatives: derivation from homogenization and initial value problem. Eur. J. Mech. A/Solid. 15, 619–642.

Anzellotti, G., 1983. Pairings between measures and bounded functions and characterization of $L^1$-approximation. Ann. Mat. Pura Appl. 135 (1), 293–318. https://doi.org/10.1007/BF01781073

Ashby, M.F., 1970. The deformation of plastically non-homogeneous materials. Philos. Mag. 21 (170), 399–424.

Bacquaert, T., Bleyer, J., Maurini, C., 2025. Regularization of softening plasticity with the cumulative plastic strain-rate gradient. J. Mech. Phys. Solid. In press.

Baratta, I.A., Dean, J.P., Dokken, J.S., Habera, M., Hale, J.S., Richardson, C.N., Rognes, M.E., Scroggs, M.W., Sime, N., Wells, G.N., 2023. DOLFINx: the next generation FEniCS problem solving environment. https://doi.org/10.5281/zenodo.10447666

Bardella, L., 2010. Size effects in phenomenological strain gradient plasticity constitutively involving the plastic spin. Int. J. Eng. Sci. 48 (5), 550–568. https://doi.org/10.1016/j.ijengsci.2009.12.003

Bardella, L., 2021. On a mixed energetic-dissipative constitutive law for non-proportional loading, with focus on small-scale plasticity. Proc. R. Soc. A: Math. Phys. Eng. Sci. 477 (2248), 20200940. https://doi.org/10.1098/rspa.2020.0940

Bardella, L., Panteghini, A., 2015. Modelling the torsion of thin metal wires by distortion gradient plasticity. J. Mech. Phys. Solids 78, 467–492. https://doi.org/10.1016/j.jmps.2015.03.003

Bilby, B.A., Bullough, R., Smith, E., 1955. Continuous distributions of dislocations: a new application of the methods of non-Riemannian geometry. Proc. R. Soc. Lond. A 231, 263–273.

Bleyer, J., 2022. Applications of conic programming in non-smooth mechanics. J. Optim. Theory Appl. , 1–33.

Chiricotto, M., Giacomelli, L., Tomassetti, G., 2012. Torsion in strain-gradient plasticity: energetic scale effects. SIAM J. Appl. Math. 72 (4), 1169–1191. https://doi.org/10.1137/120863034

Chiricotto, M., Giacomelli, L., Tomassetti, G., 2016. Dissipative scale effects in strain-gradient plasticity: the case of simple shear. SIAM J. Appl. Math. 76 (2), 688–704. https://doi.org/10.1137/15M1048227

Conti, S., Ortiz, M., 2005. Dislocation microstructures and the effective behavior of single crystals. Arch. Ration. Mech. Anal. 176 (1), 103–147. https://doi.org/10.1007/s00205-004-0353-2

Fleck, N.A., Müller, G.M., Ashby, M.F., Hutchinson, J.W., 1994. Strain gradient plasticity: theory and experiment. Acta Metall. Mater. 42 (2), 475–487. https://doi.org/10.1016/0956-7151(94)90502-9

Fleck, N.A., Willis, J.R., 2009. A mathematical basis for strain-gradient plasticity theory-part I: scalar plastic multiplier. J. Mech. Phys. Solid. 57 (1), 161–177. https://doi.org/10.1016/j.jmps.2008.09.003

Fleck, N.A., Willis, J.R., 2015. Strain gradient plasticity: energetic or dissipative? Acta Mech. Sin. 31 (4), 465–472.

Forest, S., Guéninchault, N., 2013. Inspection of free energy functions in gradient crystal plasticity. Acta Mech. Sin. 29 (6), 763–772. https://doi.org/10.1007/s10409-013-0088-0

Fortuna, M., Garroni, A., Spadaro, E., 2025. On the Read-Shockley energy for grain boundaries in poly-crystals. Commun. Pure Appl. Math. 78 (5), 121–168. https://doi.org/10.1002/cpa.22245

Garroni, A., Leoni, G., Ponsiglione, M., 2010. Gradient theory for plasticity via homogenization of discrete dislocations. J. Eur. Math. Soc. 12 (5), 1231–1266. https://doi.org/10.4171/JEMS/228

Giacomini, A., 2012. On the energetic formulation of the Gurtin and Anand model in strain gradient plasticity. Discret. Contin. Dynam. Syst. - Ser. B 17 (2), 527–552. https://doi.org/10.3934/dcdsb.2012.17.527

Gurtin, M.E., 2002. A gradient theory of single-crystal viscoplasticity that accounts for geometrically necessary dislocations. J. Mech. Phys. Solid. 50 (1), 5–32.

Gurtin, M.E., 2003. On a framework for small-deformation viscoplasticity: free energy, microforces, strain gradients. Int. J. Plast. 19 (1), 47–90. https://doi.org/10.1016/S0749-6419(01)00018-3

Gurtin, M.E., Anand, L., 2005. A theory of strain-gradient plasticity for isotropic, plastically irrotational materials. part I: small deformations. J. Mech. Phys. Solid. 53 (7), 1624–1649. https://doi.org/10.1016/j.jmps.2004.12.006

Hutchinson, J., 2000. Plasticity at the microscale. Int. J. Solid. Struct. 37, 225–238.

Jebahi, M., Forest, S., 2023. An alternative way to describe thermodynamically-consistent higher-order dissipation within strain gradient plasticity. J. Mech. Phys. Solid. 170, 105103. https://doi.org/10.1016/j.jmps.2022.105103

Kröner, E., 1958. Kontinuumstheorie der versetzungen und eigenspannungen. Ergeb. Angew. Math. 5, 1–179.

Lewintan, P., Müller, S., Neff, P., 2021. Korn inequalities for incompatible tensor fields in three space dimensions with conformally invariant dislocation energy. Calc. Var. Partial Differ. Equ. 60 (150). https://doi.org/10.1007/s00526-021-02000-x

Lussardi, L., Giacomini, A., 2008. Quasi-static evolution for a model in strain gradient plasticity. SIAM J. Math. Anal. 40 (3), 1201–1245.

Mielke, A., 2005. Evolution of rate-independent systems. In: Evolutionary Equations, Vol. II. Elsevier, pp. 461–559.

Nielsen, K.L., Hutchinson, J.W., 2021. A thermodynamically consistent theory for strain gradient plasticity without elastic gaps. J. Mech. Phys. Solid. 152, 104443. https://doi.org/10.1016/j.jmps.2021.104443

Nye, J.F., 1953. Some geometrical relations in dislocated crystals. Acta Metall. 1 (2), 153–162.

Ohno, N., Okumura, D., 2007. Higher-order stress and grain size effects due to self-energy of geometrically necessary dislocations. J. Mech. Phys. Solid. 55 (9), 1879–1898. https://doi.org/10.1016/j.jmps.2007.02.001

Ortiz, M., Repetto, E.A., 1999. Nonconvex energy minimization and dislocation structures in ductile single crystals. J. Mech. Phys. Solid. 47 (2), 397–462. https://doi.org/10.1016/S0022-5096(97)00096-3

Panteghini, A., Bardella, L., 2016. On the finite element implementation of higher-order gradient plasticity, with focus on theories based on plastic distortion incompatibility. Comput. Method. Appl. Mech. Eng. 310, 840–865. https://doi.org/10.1016/j.cma.2016.07.045

Panteghini, A., Bardella, L., 2018. On the role of higher-order conditions in distortion gradient plasticity. J. Mech. Phys. Solid. 118, 293–321. https://doi.org/10.1016/j.jmps.2018.05.019

Panteghini, A., Bardella, L., 2020. Modelling the cyclic torsion of polycrystalline micron-sized copper wires by distortion gradient plasticity. Philos. Mag. 100 (13), 1771–1783. https://doi.org/10.1080/14786435.2020.1766144

Panteghini, A., Bardella, L., Niordson, C.F., 2019. A potential for higher-order phenomenological strain gradient plasticity to predict reliable response under non-proportional loading. Proc. R. Soc. A: Math. Phys. Eng. Sci. 475 (2229), 20190258. https://doi.org/10.1098/rspa.2019.0258

Read, W.T., Shockley, W., 1950. Dislocation models of crystal grain boundaries. Phys. Rev. 78 (3), 275–289. https://doi.org/10.1103/PhysRev.78.275

Reddy, B.D., 2011. The role of dissipation and defect energy in variational formulations of problems in strain-gradient plasticity. part 1: polycrystalline plasticity. Contin. Mech. Thermodyn. 23 (6), 527–549. https://doi.org/10.1007/s00161-011-0194-9

The MOSEK optimizer API for Python. 2019. http://docs.mosek.com.

Taillard, R., Pineau, A., 1982. Room temperature tensile properties of Fe–19 wt% Cr alloys precipitation hardened by the intermetallic compound NiAl. Mater. Sci. Eng. 56, 219–231.

Wulfinghoff, S., Forest, S., Böhlke, T., 2015. Strain gradient plasticity modeling of the cyclic behavior of laminate microstructures. J. Mech. Phys. Solid. 79, 1–20. https://doi.org/10.1016/j.jmps.2015.02.008